1

MIMO Wireless Channel Modeling and Experimental Characterization

Michael A. Jensen and Jon W. Wallace

1.1 Introduction

While coding and signal processing are key elements to successful implementation of a MIMO system, the communication channel represents a major component that determines system performance. A considerable volume of work has been performed to characterize communication channels for general wireless applications. However, because MIMO systems operate at an unprecedented level of complexity to exploit the channel space-time resources, a new level of understanding of the channel space-time characteristics is required to assess the potential performance of practical multiantenna links.

This chapter will focus on experimental measurements and models aimed at characterizing the MIMO channel spatio-temporal properties. Generally, we will define this channel to include the electromagnetic propagation, antennas, and transmit/receive radio circuitry, although different measurement and modeling techniques may include all or only part of this set. When evaluating the results of these modeling and measurement campaigns, much of the discussion will focus on the pertinent properties of the propagation environment. However, an examination of the topic of MIMO channels would be incomplete without some discussion of the impact of antenna element properties – such as directivity, polarization, and mutual coupling – antenna array configuration, and radio frequency (RF) architecture on communication behavior. Therefore, we will highlight techniques for including these channel aspects in MIMO system characterization and will

Space-Time Processing for MIMO Communications Edited by A. B. Gershman and N. D. Sidiropoulos
© 2005 John Wiley & Sons, Ltd

show examples that demonstrate the impact that different design features can have on system performance.

1.1.1 MIMO system model

Figure 1.1 depicts a generic MIMO system that will serve as a reference for defining the MIMO communication channel. For this discussion and throughout this chapter, boldface uppercase and lowercase letters will represent matrices (matrix $\mathbf{H}$ with mnth element H_{mn}) and column vectors (vector $\mathbf{h}$ with mth element h_m), respectively. A stream of $Q \times 1$ vector input symbols $\mathbf{b}^{(k)}$, where k is a time index, are fed into a space-time encoder, generating a stream of $N_T \times 1$ complex vectors $\mathbf{x}^{(k)}$, where N_T represents the number of transmit antennas. Pulse shaping filters transform each element of the vector to create a $N_T \times 1$ time-domain signal vector $\mathbf{x}(t)$, which is up-converted to a suitable transmission carrier (RF, microwave, optical, acoustic). The resulting signal vector $\mathbf{x}_A(t)$ drives the transmit transducer array (antennas, lasers, speakers), which in turn radiates energy into the propagation environment.

The function $h_P(t, \tau, \theta_R, \phi_R, \theta_T, \phi_T)$ represents the impulse response relating field radiated by the transmit array to the field incident on the receive array. The dependence on time t suggests that this impulse response is time variant because of motion of scatterers within the propagation environment or motion of the transmitter and receiver. The variable τ represents the time delay relative to the excitation time t. We assume a finite impulse response, so that $h_P(t, \tau, \theta_R, \phi_R, \theta_T, \phi_T) = 0$ for $\tau > \tau_0$. We also assume that $h_P(t, \tau, \theta_R, \phi_R, \theta_T, \phi_T)$ remains constant over a time interval (in t) of duration τ_0 so that over a single transmission, the physical channel can be treated as a linear, time-invariant system.

Assume now that the input signal $\mathbf{x}_A(t)$ creates the field $x_P(t, \theta_T, \phi_T)$ radiated from the transmit array, where (θ_T, ϕ_T) denote the elevation and azimuthal angles taken with respect to the coordinate frame of the transmit array. At the receive array, the field distribution $y_P(t, \theta_R, \phi_R)$, where (θ_R, ϕ_R) represent angles referenced to the receive array coordinate frame, and can be expressed as the convolution

$$y_P(t, \theta_R, \phi_R) = \int_0^{2\pi} \int_0^{\pi} \int_{-\infty}^{\infty} h_P(t, \tau, \theta_R, \phi_R, \theta_T, \phi_T) x_P(t - \tau, \theta_T, \phi_T) \sin\theta_T \, d\tau \, d\theta_T \, d\phi_T \tag{1.1}$$

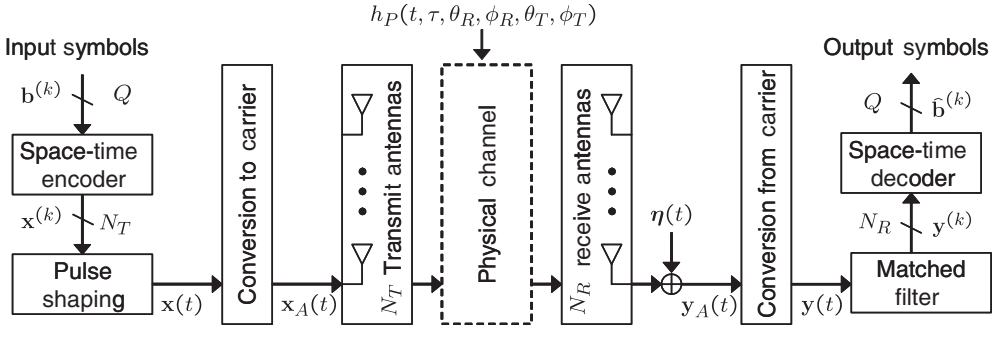

Figure 1.1 A generic MIMO communication system.

The N_R-element receive array then samples this field and generates the $N_R \times 1$ signal vector $\mathbf{y}'_A(t)$ at the array terminals. Noise in the system is typically generated in the physical propagation channel (interference) and the receiver front-end electronics (thermal noise). To simplify the discussion, we will lump all additive noise into a single contribution represented by the $N_R \times 1$ vector $\boldsymbol{\eta}(t)$ that is injected at the receive antenna terminals. The resulting signal plus noise vector $\mathbf{y}_A(t)$ is then downconverted to produce the $N_R \times 1$ baseband output vector $\mathbf{y}(t)$. Finally, $\mathbf{y}(t)$ is passed through a matched filter whose output is sampled once per symbol to produce $\mathbf{y}^{(k)}$, after which the space-time decoder produces estimates $\hat{\mathbf{b}}^{(k)}$ of the originally transmitted symbols.

This chapter focuses on the characteristics of the channel, although the specific definition of this channel can vary depending on the goal of the analysis. For example, in some cases we wish to focus on the physical channel impulse response and use it to generate a channel matrix relating the signals $\mathbf{x}_A(t)$ and $\mathbf{y}_A(t)$. A common assumption will be that all scattering in the propagation channel is in the far field and that a discrete number of propagation "paths" connects the transmit and receive arrays. Under this assumption, the physical channel response for L paths may be written as

$$h_P(t, \tau, \theta_R, \phi_R, \theta_T, \phi_T) = \sum_{\ell=1}^{L} A_\ell \delta(\tau - \tau_\ell)\delta(\theta_T - \theta_{T,\ell}) \times \delta(\phi_T - \phi_{T,\ell})\delta(\theta_R - \theta_{R,\ell})\delta(\phi_R - \phi_{R,\ell}), \tag{1.2}$$

where A_ℓ is the gain of the ℓth path with angle of departure (AOD) $(\theta_{T,\ell}, \phi_{T,\ell})$, angle of arrival (AOA) $(\theta_{R,\ell}, \phi_{R,\ell})$, and time of arrival (TOA) τ_ℓ. The term $\delta(\cdot)$ represents the Dirac delta function. The time variation of the channel is included by making the parameters of the multipaths $(L,\ A_\ell,\ \tau_\ell,\ \theta_{T,\ell}, \ldots)$ time dependent. To use this response to relate $\mathbf{x}_A(t)$ to $\mathbf{y}_A(t)$, it is easier to proceed in the frequency domain. We take the Fourier transform of the relevant signals to obtain $\tilde{\mathbf{x}}_A(\omega)$, $\tilde{\mathbf{y}}_A(\omega)$, and $\tilde{\boldsymbol{\eta}}(\omega)$, and take the Fourier transform of h_P with respect to the delay variable τ to obtain $\tilde{h}_P(t, \omega, \theta_R, \phi_R, \theta_T, \phi_T)$ where ω is the radian frequency. Assuming single-polarization array elements, the frequency domain radiation patterns of the nth transmit and mth receive array elements are $e_{T,n}(\omega, \theta_T, \phi_T)$ and $e_{R,m}(\omega, \theta_R, \phi_R)$, respectively. We must convolve these patterns with $\tilde{h}_P$ in the angular coordinates to obtain

$$\tilde{\mathbf{y}}_A(\omega) = \mathbf{H}_P(\omega)\tilde{\mathbf{x}}_A(\omega) + \tilde{\boldsymbol{\eta}}(\omega) \tag{1.3}$$

where

$$H_{P,mn}(\omega) = \sum_{\ell=1}^{L} \beta_\ell\ e_{R,m}(\omega, \theta_{R,\ell}, \phi_{R,\ell}) e_{T,n}(\omega, \theta_{T,\ell}, \phi_{T,\ell}) \tag{1.4}$$

and $\beta_\ell = A_\ell \exp\{-j\omega\tau_\ell\}$ is the complex gain of the ℓth path. $\mathbf{H}_P(\omega)$ is referred to as the *channel transfer matrix* or simply *channel matrix*. Although this representation is usually inconvenient for closed-form analysis of space-time code behavior, it explicitly uses the antenna properties in constructing the channel matrix, and therefore facilitates examination of a variety of antenna configurations for a single physical propagation channel. Also, because it is based on the physical channel impulse response, it is appropriate for wideband or *frequency selective* channels for which the elements of $\mathbf{H}_P(\omega)$ vary significantly over the bandwidth of interest.

While the physical channel model in (1.3) is useful for certain cases, in most signal-processing analyses the channel is taken to relate the input to the pulse shaping block $\mathbf{x}^{(k)}$ to the output of the matched filter $\mathbf{y}^{(k)}$. This model is typically used for cases where the frequency domain channel transfer function remains approximately constant over the bandwidth of the transmitted waveform, often referred to as the *frequency nonselective* or *flat fading* scenario. In this case, the frequency domain transfer functions can be treated as complex constants that simply scale the complex input symbols. We can therefore write the input/output relationship as

$$\mathbf{y}^{(k)} = \mathbf{H}^{(k)}\mathbf{x}^{(k)} + \boldsymbol{\eta}^{(k)} \tag{1.5}$$

where $\boldsymbol{\eta}^{(k)}$ denotes the noise that has passed through the receiver and has been sampled at the matched-filter output. The term $\mathbf{H}^{(k)}$ represents the channel matrix for the kth transmitted symbol, with the superscript explicitly indicating that the channel can change over time. Throughout this chapter, we will sometimes drop this superscript for convenience. We emphasize here that $\mathbf{H}^{(k)}$ is based on the value of $\mathbf{H}_P(\omega)$ evaluated at the carrier frequency but includes the additional effects of the transmit and receive electronics. This model forms the basis of the random matrix models covered in Section 1.3.1 and is very convenient for closed-form analysis. The main drawbacks of this approach are the modeling inaccuracy, the difficulty of specifying $\mathbf{H}^{(k)}$ for all systems of practical interest, and the fact that it does not lend itself to the description of frequency selective channels.

The discussion thus far has ignored certain aspects of the MIMO system that may be important in some applications. For example, realistic microwave components will experience complicated interactions due to coupling and noise, factors that may be treated with advanced network models as detailed in Section 1.4.3. The effects of non-ideal matched filters and sampling may also be of interest, which can be analyzed with the appropriate level of modeling detail [1].

1.1.2 Channel normalization

Consider the channel model in (1.5) where the noise $\boldsymbol{\eta}^{(k)}$ is assumed to be a random vector with zero-mean complex normal entries and covariance $\sigma_\eta^2\mathbf{I}$, where $\mathbf{I}$ is the identity matrix. The average noise power in each receiver is therefore given by the variance σ_η^2 of the complex random variables. The signal power averaged in time as well as over all receive ports is given as

$$P_R = \frac{1}{N_R}\,\mathrm{E}\left\{\mathbf{x}^{(k)H}\mathbf{H}^{(k)H}\mathbf{H}^{(k)}\mathbf{x}^{(k)}\right\} = \frac{1}{N_R}\mathrm{Tr}\left(\,\mathrm{E}\left\{\mathbf{x}^{(k)}\mathbf{x}^{(k)H}\right\}\,\mathrm{E}\left\{\mathbf{H}^{(k)H}\mathbf{H}^{(k)}\right\}\right), \tag{1.6}$$

where $\mathrm{E}\{\cdot\}$ denotes expectation, $\{\cdot\}^H$ represents a matrix conjugate transpose and $\mathrm{Tr}(\cdot)$ is a matrix trace. We have used the statistical independence of the signal $\mathbf{x}^{(k)}$ and channel matrix $\mathbf{H}^{(k)}$ to manipulate this expression. If the transmitter divides the total transmit power P_T equally across statistically independent streams on the multiple antennas, $\mathrm{E}\left\{\mathbf{x}^{(k)}\mathbf{x}^{(k)H}\right\} = (P_T/N_T)\mathbf{I}$. If the expectation $\mathrm{E}\left\{\mathbf{H}^{(k)H}\mathbf{H}^{(k)}\right\}$ is approximated using a sample mean over a series $1 \le k \le K$, the average received signal power is

$$P_R = \frac{P_T}{N_T N_R K}\sum_{k=1}^{K}\left\|\mathbf{H}^{(k)}\right\|_F^2, \tag{1.7}$$

where $\|\cdot\|_F$ is the Frobenius norm. The signal-to-noise ratio (SNR) averaged in time as well as over all receive ports is therefore

$$\mathrm{SNR} = \frac{P_T}{\sigma_\eta^2} \underbrace{\frac{1}{N_T N_R K} \sum_{k=1}^{K} \left\| \mathbf{H}^{(k)} \right\|_F^2}_{\Upsilon}. \tag{1.8}$$

We recognize that Υ represents the average of the power gains between each pair of transmit and receive antennas. The resulting SNR is equivalent to what would be obtained if the power were transmitted between a single pair of antennas with channel power gain Υ. We therefore refer to (1.8) as the **single-input single-output** (SISO) SNR.

When performing simulations and analyses using channel matrices obtained from measurements or models, it is often useful to be able to properly scale $\mathbf{H}^{(k)}$ to achieve a specified average SNR. We therefore define a new set of channel matrices $\mathbf{H}_0^{(k)} = \Psi \mathbf{H}^{(k)}$, where Ψ is a normalizing constant. To achieve a given average SNR, Ψ should be chosen according to

$$\Psi^2 = \mathrm{SNR} \frac{\sigma_\eta^2}{P_T} \frac{N_T N_R K}{\sum_{\kappa=1}^{K} \left\| \mathbf{H}^{(\kappa)} \right\|_F^2}. \tag{1.9}$$

If $K = 1$, this implies that each individual channel matrix is normalized to have the specified SNR. If $K > 1$, the average SNR over the group of K matrices will be as specified, although the SNR for each individual matrix will fluctuate about this mean value. This allows investigation of the relative variations in received signal strength over an ensemble of measurements or simulations.

1.2 MIMO Channel Measurement

The most direct way to gain an understanding of the MIMO wireless channel is to experimentally measure the $N_R \times N_T$ channel matrix $\mathbf{H}$. These measurements include the effects of the RF subsystems and the antennas, and therefore the results are dependent on the array configurations used. A variety of such measurements have been reported [2–11], and results obtained include channel capacity, signal correlation structure (in space, frequency, and time), channel matrix rank, path loss, delay spread, and a variety of other quantities. *True array* systems, where all antennas operate simultaneously, most closely model real-world MIMO communication, and can accommodate channels that vary in time. However, the implementation of such a system comes at significant cost and complexity because of the requirement of multiple parallel transmit and receive electronic subsystems.

Other measurement systems are based on either *switched array* or *virtual array* architectures. Switched array designs use a single transmitter and single receiver, sequentially connecting all array elements to the electronics using high-speed switches [12, 13]. Switching times for such systems are necessarily low (2 μs to 100 ms) to allow the measurement over all antenna pairs to be completed before the channel changes. Virtual array architectures use precision displacement (or rotation) of a single antenna element rather than a set of fixed antennas connected via switches [14–16]. Although this method has the advantage of eliminating mutual coupling, a complete channel matrix measurement often takes several

seconds or minutes. Therefore, such a technique is appropriate for fixed indoor measurement campaigns when the channel remains constant for relatively long periods.

In this section, we will provide details regarding a true array system for direct transfer matrix measurement and illustrate MIMO performance for representative propagation environments. While the approach taken here is not unique, particularly with regard to the modulation constellation used and specific system architecture, the system shown is representative of typical platforms used in MIMO channel probing. Following the discussion of the system, we will discuss additional processing that can be accomplished using MIMO system measurements to allow estimation of the physical multipath characteristics associated with the propagation channel.

1.2.1 Measurement system

The platform detailed here, as depicted in Figure 1.2, uses a narrowband MIMO communications system operating at a center frequency of 2.45 GHz. Up to 16 unique binary sequences are constructed using a shift-generator employing a maximal length sequence polynomial [17] and then output using a digital pattern generator ($\pm$5V). The sequences are individually multiplied by a common microwave local oscillator (LO) signal to generate binary phase shift keyed (BPSK) waveforms that are amplified and fed to one of the N_T transmit antennas. The signal on each of the $N_R \leq 16$ receive antennas is amplified, downconverted to an intermediate frequency (IF), filtered, and sampled on a 16-channel 1.25 Msample/s analog-to-digital (A/D) conversion card for storage and postprocessing. The system is calibrated before each measurement to remove the effects of unequal complex gains in the electronics.

Once the IF data is collected, postprocessing is used to perform carrier and symbol timing recovery and code synchronization. To locate the start of the codes, the signal from one of the N_R receive antennas is correlated with a baseband representation of one of the transmit codes. A Fast Fourier Transform (FFT) of this result produces a peak at the IF when the selected transmit code is aligned with the same code in the receive signal. The search for this alignment is simplified by using shortened correlating codes and coarse steps at the beginning of the process and adaptively reducing the step size and switching to full-length codes as the search converges. Additionally, if the specified code is weakly represented in the received signal chosen, the maximum correlation may not occur at code alignment. The

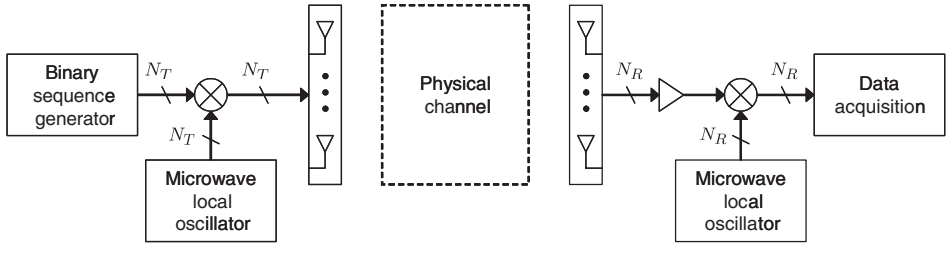

Figure 1.2 High level system diagram of the narrowband wireless MIMO measurement system.

procedure therefore searches over all combinations of receive channel and code to ensure accurate code synchronization.

The IF is approximately given by the frequency at which the peak in the FFT occurs. This frequency estimate is refined using a simple optimization that maximizes the magnitude of the Discrete Time Fourier Transform (DTFT) of the known aligned code multiplied by the receive signal (despread signal). Subsequently, the waveform generated by moving a window along the despread signal is correlated against a complex sinusoid at the IF, and the phase of the result is taken as the carrier phase at the center of the recovery window. A moving average filter is finally used to smooth this phase estimate.

With the carrier and timing recovery performed, the channel transfer matrix can be extracted from the data using a maximum likelihood (ML) channel inversion technique. Let A_{mn} and ϕ_{mn} represent the amplitude and phase, respectively, of the signal from transmit antenna n as observed on receive antenna m. Therefore, the estimate of the mnth element of the transfer matrix is $\widehat{H}_{mn} = A_{mn}e^{j\phi_{mn}} = H_{mn}^R + jH_{mn}^I$, where H_{mn}^R and H_{mn}^I represent the real and imaginary parts of $\widehat{H}_{mn}$, respectively. If $f_n^{(k)}$ represents the kth sample of the code from the nth transmit antenna, the discrete signal at the port of the mth receive antenna is given as

$$y_m^{(k)} = \sum_{n=1}^{N_T} A_{mn} f_n^{(k)} \cos(\varpi_0 k + \phi^{(k)} + \phi_{mn}) + \eta_m^{(k)} \tag{1.10}$$

where ϖ_0 is the discrete (recovered) carrier frequency, $\phi^{(k)}$ is the randomly varying carrier phase, and $\eta_m^{(k)}$ represents the discrete noise sample that is assumed to be spectrally white with a zero-mean Gaussian amplitude distribution.

We now consider a sequence of $k_2 - k_1 + 1$ samples, which is the length of the code multiplied by the number of samples per symbol. If $\hat{y}_m^{(k)}$ represents the observed signal, then the ML estimate of the channel transfer function results from finding the values of $\widehat{H}_{mn}$ that minimize

$$T_m = \sum_{k=k_1}^{k_2} \left| \hat{y}_m^{(k)} - \sum_{n=1}^{N_T} \left\{ H_{mn}^R \cos(\varpi_0 k + \phi^{(k)}) - H_{mn}^I \sin(\varpi_0 k + \phi^{(k)}) \right\} f_n^{(k)} \right|^2 . \tag{1.11}$$

Taking the derivative of T_m with respect to both H_{ms}^R and H_{ms}^I, $1 \le s \le N_T$, and setting the result to zero produces the equations

$$2 \sum_{k=k_1}^{k_2} \hat{y}_m^{(k)} f_s^{(k)} \cos(\varpi_0 k + \phi^{(k)}) = \sum_{k=k_1}^{k_2} \sum_{n=1}^{N_T} f_n^{(k)} f_s^{(k)} \left\{ H_{mn}^R (1 + \alpha_k) - H_{mn}^I \beta_k \right\} \tag{1.12}$$

$$2 \sum_{k=k_1}^{k_2} \hat{y}_m^{(k)} f_s^{(k)} \sin(\varpi_0 k + \phi^{(k)}) = \sum_{k=k_1}^{k_2} \sum_{n=1}^{N_T} f_n^{(k)} f_s^{(k)} \left\{ H_{mn}^I (1 - \alpha_k) - H_{mn}^R \beta_k \right\} \tag{1.13}$$

where $1 \le m \le N_R$, $\alpha_k = \cos[2(\varpi_0 k + \phi^{(k)})]$ and $\beta_k = \sin[2(\varpi_0 k + \phi^{(k)})]$. For a given value of m, these equations form a linear system that can be solved for the unknown coefficients H_{mn}^R and H_{mn}^I.

1.2.2 Channel matrix characteristics

Measurements were taken in a building constructed with cinder-block partition walls and steel-reinforced concrete structural walls and containing classrooms, laboratories, and several small offices. Data were collected using 1000-bit binary codes at a chip rate of 12.5 kbps, producing one channel matrix estimate every 80 ms (representing the average channel response over the code length). Because channel changes occur on the timescales of relatively slow physical motion (people moving, doors closing, etc.), this sample interval is adequate for the indoor environment under investigation. For all measurements, the SISO SNR is set to 20 dB and, unless explicitly stated, is computed for $K = 1$ in (1.9).

The three different measurement scenarios considered here are listed in the table below. In this list, "Room A" and "Room B" are central labs separated by a hallway (designated as "Hall"), while "Many Rooms" indicates that the receiver was placed at several locations in different rooms. The arrays were all linear with the element type and spacing as indicated in the table, where λ represents the free-space wavelength of the excitation. Multiple 10-second data records (200–700) were taken for each scenario.

Name ($N_R \times N_T$)	**Transmitter location**	**Receiver location**	**Antenna elements**	**Spacing**
4×4-V	Room A	Many rooms	4 vertical monopoles	$\lambda/2$
4×4-VH	Hall	Room B	2 dual-polarization patches	$\lambda/2$
10×10-V	Many rooms	Many rooms	10 vertical monopoles	$\lambda/4$

For the data collected, the marginal probability density functions (PDF) for the magnitude and phase of the elements of $\mathbf{H}$ can be estimated using the histograms

$$p_{\text{mag}}[x] = \frac{1}{K N_R N_T \Delta x} \underset{K,N_R,N_T}{\text{HIST}} (|H_{mn}^{(k)}|, \Delta x) \tag{1.14}$$

$$p_{\text{pha}}[x] = \frac{1}{K N_R N_T \Delta x} \underset{K,N_R,N_T}{\text{HIST}} (\angle H_{mn}^{(k)}, \Delta x) \tag{1.15}$$

where $\text{HIST}(f, \Delta x)$ represents a histogram of the function f with bins of size Δx and K is the number of transfer matrix samples. These histograms are computed by treating each combination of matrix sample, transmit antenna, and receive antenna as an observation. Figure 1.3 shows the empirical PDFs for sets 4×4-V (subplots (a) and (b)) and 10×10-V (subplots (c) and (d)). The fitting curves for magnitude and phase are the Rayleigh PDF with a variance of 0.5 and the uniform distribution on $[-\pi,\ \pi]$, respectively. The agreement between the analytical and empirical PDFs is excellent.

The timescale of channel variation is an important consideration since this indicates the frequency with which channel estimation (and perhaps channel feedback) must occur to maintain reliable communication. To assess this temporal variability, we can examine the temporal autocorrelation function for each element of the transfer matrix. Assuming the channel matrix elements are zero mean, the average autocorrelation is given as

$$X_\ell = \text{E}\left\{ H_{mn}^{(k)} H_{mn}^{*(k+\ell)} \right\} \tag{1.16}$$

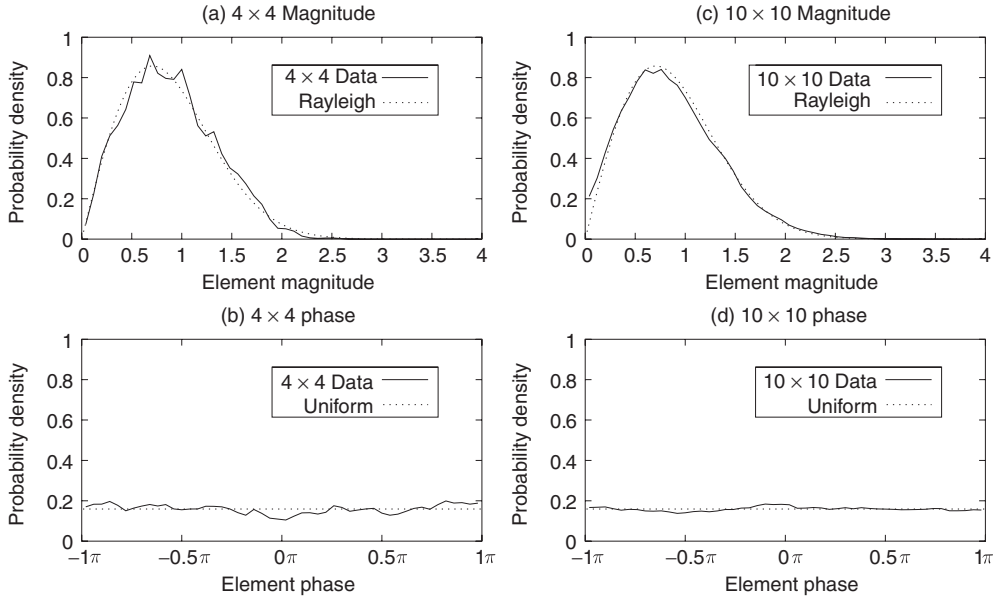

Figure 1.3 Empirical PDFs for the magnitude and phase of the 4×4 $\mathbf{H}$ matrix elements compared with Rayleigh and uniform PDFs, respectively.

where ℓ is a sample shift, $\{\cdot\}^*$ denotes complex conjugate, and the expectation is approximated as a sample mean over all combinations of transmit antenna (n), receive antenna (m), and starting time sample (k). The temporal correlation coefficient is then given by $\rho_\ell = X_\ell / X_0$. Figure 1.4 plots the magnitude of ρ_ℓ over a period of 5 seconds for the two different 4×4 data sets. For all measurements, the correlation remains relatively high, indicating that the channel remains relatively stationary in time. The more dramatic decrease in ρ_ℓ for set 4×4-VH is likely a consequence of the fact that this data was taken during the day when activity was high, while the data for set 4×4-V was taken while activity was low.

The correlation between the signals on the antennas is another important indicator of performance since lower signal correlation tends to produce higher average channel capacity. We assume that the correlation functions at transmit and receive antennas are shift-invariant, and we therefore treat all pairs of antennas with the same spacing as independent observations. This allows us to define the transmit and receive correlation functions

$$R_{T,q} = \frac{1}{N_R N_q} \sum_{n=1}^{N_q} \sum_{m=1}^{N_R} \mathrm{E}\left\{ H_{mn} H_{m,n+q}^* \right\} \tag{1.17}$$

$$R_{R,p} = \frac{1}{N_T N_p} \sum_{n=1}^{N_T} \sum_{m=1}^{N_p} \mathrm{E}\left\{ H_{mn} H_{m+p,n}^* \right\}. \tag{1.18}$$

where N_q (N_p) represents the number of unique pairs of transmit (receive) antennas separated by the distance $q\Delta z$ ($p\Delta z$), where Δz represents the antenna element spacing. For the

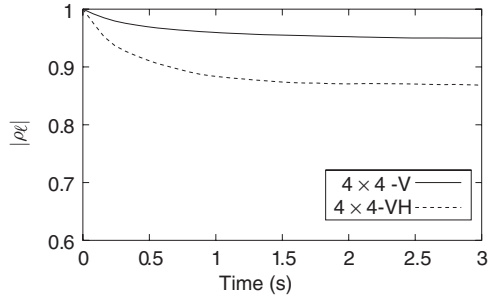

Figure 1.4 Temporal correlation coefficient over a 5-second interval for the two 4×4 data sets.

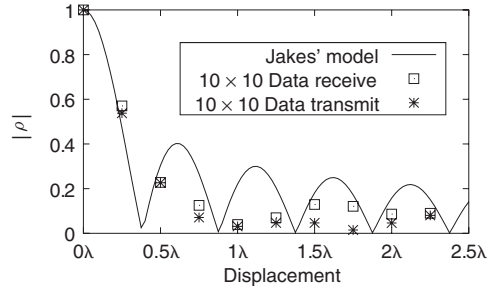

Figure 1.5 Magnitude of the shift-invariant transmit and receive spatial correlation coefficients compared with Jakes' model.

measured data, the expectation is replaced by an average over all time samples. The transmit and receive correlation coefficients are then constructed using $\rho_{T,q} = R_{T,q}/R_{T,0}$ and $\rho_{R,p} = R_{R,p}/R_{R,0}$, respectively. Figure 1.5 shows the shift-invariant spatial transmit and receive correlation coefficient computed from the 10×10 data versus antenna separation $p\Delta z$ and $q\Delta z$. For comparison, results obtained from Jakes' model [18], where an assumed uniform distribution on multipath arrival angles leads to $R_{R,s} = R_{T,s} = J_0(2\pi s\Delta z/\lambda)$ with $J_0(\cdot)$ the Bessel function of order zero, are also included. These results show that for antenna spacings where measurements were performed, Jakes' model predicts the trends observed in the data.

Finally, we examine the channel capacities associated with the measured channel matrices. Capacities are computed using the water-filling solution [19], which provides the upper bound on data throughput across the channel under the condition that the transmitter is aware of the channel matrix $\mathbf{H}$. For this study, we consider transmit and receive arrays each confined to a 2.25λ aperture and consisting of 2, 4, and 10 equally spaced monopoles. Figure 1.6 shows the complementary cumulative distribution functions (CCDF) of capacity for these scenarios. Also, Monte Carlo simulations were performed to obtain capacity CCDFs for channel matrices whose elements are independent, identically distributed (i.i.d.)

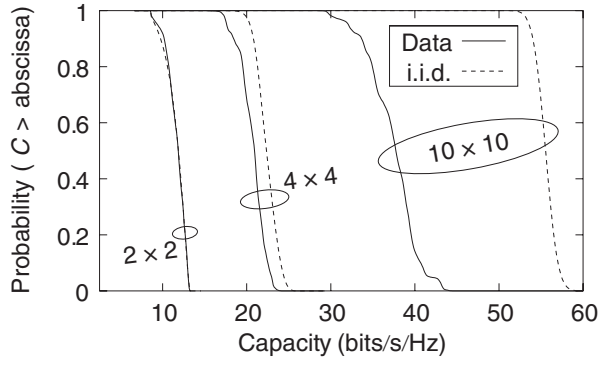

Figure 1.6 Complementary cumulative distribution functions of capacity for transmit/receive arrays of increasing number of elements. The array length is 2.25 λ for all cases.

zero-mean complex Gaussian random variables, as outlined in Section 1.3.1. The agreement between the measured and modeled 2×2 channels is excellent because of the very wide separation of the antennas (2.25λ). However, as the array size increases, the simulated capacity continues to grow while the measured capacity *per antenna* decreases because of higher correlation between adjacent elements.

The capacity results of Figure 1.6 neglect differences in received SNR among the different channel measurements since each channel matrix realization is independently normalized to achieve the 20 dB average SISO SNR. To examine the impact of this effect more closely, the 10×10 linear arrays of monopoles with $\lambda/4$ element separation were deployed in a number of different locations. Figure 1.7 shows the different locations, where each arrow points from transmit to receive location. The top number in the circle on each arrow represents the capacity obtained when the measured channel matrix is independently normalized to achieve 20 dB SISO SNR ($K = 1$ in (1.9)). The second number (in italics) represents the capacity obtained when the normalization is applied over *all* $\mathbf{H}$ matrices considered in the study. Often, when the separation between transmit and receive is large (E $\rightarrow$ C, for example), the capacity degradation observed when propagation loss is included is significant. In other cases (such as G $\rightarrow$ D), the capacity computed with propagation loss included actually increases because of the high SNR resulting from the small separation between transmit and receive.

1.2.3 Multipath estimation

Another philosophy regarding MIMO channel characterization is to directly describe the properties of the physical multipath propagation channel, independent of the measurement antennas. Most such system-independent representations use the double-directional channel concept [20, 21] in which the AOD, AOA, TOA, and complex gain of each multipath component are specified. Once this information is known, the performance of arbitrary antennas and array configurations placed in the propagation channel may be analyzed by creating a channel transfer function from the measured channel response as in (1.4).

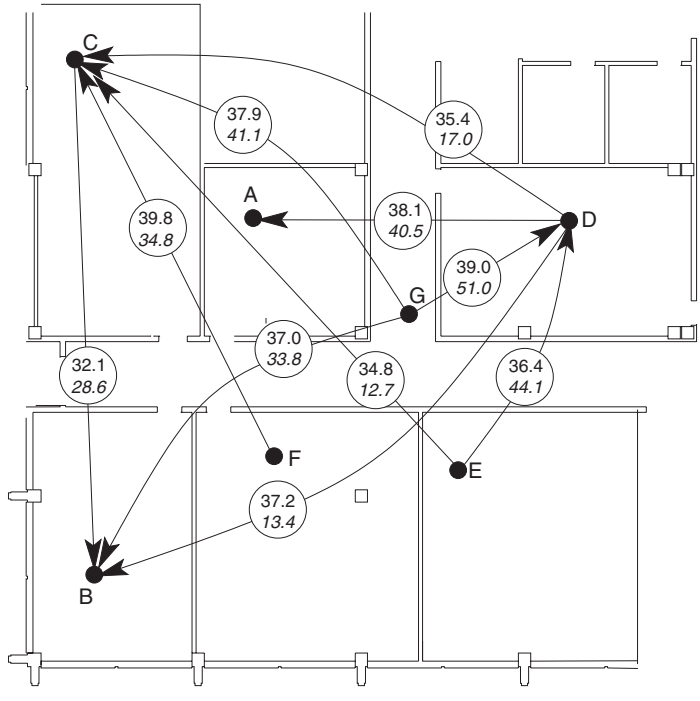

Figure 1.7 Study showing the impact of including the effects of propagation loss in computing the capacity. Arrows are drawn from transmit to receive positions. The top and bottom number in each circle give capacity without and with propagation loss, respectively.

Conceptually, the simplest method for measuring the physical channel response is to use two steerable (manually or electronically) high-gain antennas. For each fixed position of the transmit beam, the receive beam is rotated through 360°, thus mapping out the physical channel response as a function of azimuth angle at the transmit and receive antenna locations [22, 23]. Typically, broad probing bandwidths are used to allow resolution of the multipath plane waves in time as well as angle. The resolution of this system is proportional to the antenna aperture (for directional estimation) and the bandwidth (for delay estimation). Unfortunately, because of the long time required to rotate the antennas, the use of such a measurement arrangement is limited to channels that are highly stationary.

To avoid the difficulties with steered-antenna systems, it is more common and convenient to use the same measurement architecture as is used to directly measure the channel transfer matrix (Figure 1.2). However, attempting to extract more detailed information about the propagation environment requires a much higher level of postprocessing. Assuming far-field scattering, we begin with relationship (1.4), where the radiation patterns for the antennas are known. Our goal is then to estimate the number of arrivals L, the directions of departure $(\theta_{T,\ell}, \phi_{T,\ell})$ and arrival $(\theta_{R,\ell}, \phi_{R,\ell})$, and times of arrival τ_ℓ. Theoretically, this information could be obtained by applying an optimal ML estimator. However, since many practical scenarios will have tens to hundreds of multipath components, this method quickly becomes computationally intractable.

On the other hand, subspace parametric estimators like ESPRIT provide an efficient method of obtaining the multipath parameters without the need for computationally expensive search algorithms. The resolution of such methods is not limited by the size of the array aperture, as long as the number of antenna elements is larger than the number of multipaths. These estimators usually require knowledge about the number of multipath components, which can be obtained by a simple "Scree" plot or minimum description length criterion [24–26].

While this double-directional channel characterization is very powerful, there are several basic problems inherent to this type of channel estimation. First, the narrowband assumption in the signal space model precludes the direct use of wideband data. Thus, angles and times of arrival must be estimated independently, possibly leading to suboptimal parameter estimation. Second, in their original form, parametric methods such as ESPRIT only estimate directions of arrival and departure separately, and therefore the estimator does not pair these parameters to achieve an optimal fit to the data. This problem can be overcome by either applying alternating conventional beamforming and parametric estimation [20] or by applying advanced joint diagonalization methods [27, 28]. Third, in cases where there is near-field or diffuse scattering [21, 29] the parametric plane-wave model is incorrect, leading to inaccurate estimation results. However, in cases where these problems are not severe, the wealth of information obtained from these estimation procedures gives deep insight into the behavior of MIMO channels and allows development of powerful channel models that accurately capture the physics of the propagation environment.

1.3 MIMO Channel Models

Direct channel measurements provide definitive information regarding the potential performance of MIMO wireless systems. However, owing to the cost and complexity of conducting such measurement campaigns, it is important to have channel models available that accurately capture the key behaviors observed in the experimental data [30–33, 1]. Modeling of SISO and MIMO wireless systems has also been addressed extensively by several working groups as part of European COST Actions (COST-231 [34], COST-259 [21], and COST-273), whose goal is to develop and standardize propagation models.

When accurate, these models facilitate performance assessment of potential space-time coding approaches in realistic propagation environments. There are a variety of different approaches used for modeling the MIMO wireless channel. This section outlines several of the most widely used techniques and discusses their relative complexity and accuracy tradeoffs.

1.3.1 Random matrix models

Perhaps the simplest strategy for modeling the MIMO channel uses the relationship (1.5), where the effects of antennas, the physical channel, and matched filtering have been lumped into a single matrix $\mathbf{H}^{(k)}$. Throughout this section, the superscript (k) will be dropped for simplicity. The simple linear relationship allows for convenient closed-form analysis, at the expense of possibly reduced modeling accuracy. Also, any model developed with this method will likely depend on assumptions made about the specific antenna types and

array configurations, a limitation that is overcome by the more advanced path-based models presented in Section 1.3.3.

The multivariate complex normal distribution

The multivariate complex normal (MCN) distribution has been used extensively in early as well as recent MIMO channel modeling efforts, because of simplicity and compatibility with single-antenna Rayleigh fading. In fact, the measured data in Figure 1.3 shows that the channel matrix elements have magnitude and phase distributions that fit well to Rayleigh and uniform distributions, respectively, indicating that these matrix entries can be treated as complex normal random variables.

From a modeling perspective, the elements of the channel matrix $\mathbf{H}$ are stacked into a vector $\mathbf{h}$, whose statistics are governed by the MCN distribution. The PDF of an MCN distribution may be defined as

$$f(\mathbf{h}) = \frac{1}{\pi^N \det\{\mathbf{R}\}} \exp[-(\mathbf{h}-\boldsymbol{\mu})^H \mathbf{R}^{-1}(\mathbf{h}-\boldsymbol{\mu})], \tag{1.19}$$

where

$$\mathbf{R} = \mathrm{E}\left\{(\mathbf{h}-\boldsymbol{\mu})(\mathbf{h}-\boldsymbol{\mu})^H\right\} \tag{1.20}$$

is the (non-singular) covariance matrix of $\mathbf{h}$, N is the dimensionality of $\mathbf{R}$, $\boldsymbol{\mu}$ is the mean of $\mathbf{h}$, and $\det\{\cdot\}$ is a determinant. In the special case where the covariance $\mathbf{R}$ is singular, the distribution is better defined in terms of the characteristic function. This distribution models the case of Rayleigh fading when the mean channel vector $\boldsymbol{\mu}$ is set to zero. If $\boldsymbol{\mu}$ is nonzero, a non-fading or line-of-sight component is included and the resulting channel matrix describes a Rician fading environment.

Covariance matrices and simplifying assumptions

The zero mean MCN distribution is completely characterized by the covariance matrix $\mathbf{R}$ in (1.20). For this discussion, it will be convenient to represent the covariance as a tensor indexed by four (rather than two) indices according to

$$R_{mn,pq} = \mathrm{E}\left\{H_{mn} H_{pq}^*\right\}. \tag{1.21}$$

This form is equivalent to (1.20), since m and n combine and p and q combine to form row and column indices, respectively, of $\mathbf{R}$.

While defining the full covariance matrix $\mathbf{R}$ presents no difficulty conceptually, as the number of antennas grows, the number of covariance matrix elements can become prohibitive from a modeling standpoint. Therefore, the simplifying assumptions of *separability* and *shift invariance* can be applied to reduce the number of parameters in the MCN model.

Separability assumes that the full covariance matrix may be written as a product of transmit covariance ($\mathbf{R}_T$) and receive covariance ($\mathbf{R}_R$) or

$$R_{mn,pq} = R_{R,mp} R_{T,nq}, \tag{1.22}$$

where $\mathbf{R}_T$ and $\mathbf{R}_R$ are defined in (1.17) and (1.18). When this assumption is valid, the transmit and receive covariance matrices can be computed from the full covariance matrix as

$$R_{T,nq} = \frac{1}{\alpha} \sum_{m=1}^{N_R} R_{mn,mq} \tag{1.23}$$

$$R_{R,mp} = \frac{1}{\beta} \sum_{n=1}^{N_T} R_{mn,pn}, \tag{1.24}$$

where α and β are chosen such that

$$\alpha\beta = \sum_{k_1=1}^{N_R} \sum_{k_2=1}^{N_T} R_{k_1k_2,k_1k_2}. \tag{1.25}$$

In the case where $\mathbf{R}$ is a correlation coefficient matrix, we may choose $\alpha = N_R$ and $\beta = N_T$. The separability assumption is commonly known as the *Kronecker model* in recent literature, since we may write

$$\mathbf{R} = \mathbf{R}_T \otimes \mathbf{R}_R, \tag{1.26}$$

$$\mathbf{R}_T = \frac{1}{\alpha} \mathrm{E}\left\{\mathbf{H}^H\mathbf{H}\right\}^T, \tag{1.27}$$

$$\mathbf{R}_R = \frac{1}{\beta} \mathrm{E}\left\{\mathbf{H}\mathbf{H}^H\right\}, \tag{1.28}$$

$$\alpha\beta = \mathrm{Tr}(\mathbf{R}) = \mathrm{E}\left\{\|\mathbf{H}\|_F^2\right\}, \tag{1.29}$$

where $\{\cdot\}^T$ is a matrix transpose. The separable Kronecker model appeared in early MIMO modeling work [31, 35, 7] and has demonstrated good agreement for systems with relatively few antennas (2 or 3). However, for systems with a large number of antennas, the Kronecker relationship becomes an artificial constraint that leads to modeling inaccuracy [36, 37].

Shift invariance assumes that the covariance matrix is only a function of antenna separation and not absolute antenna location [24]. The relationship between the full covariance and shift-invariant covariance $\mathbf{R}^S$ is

$$R_{mn,pq} = R^S_{m-p,n-q}. \tag{1.30}$$

For example, shift invariance is valid for the case of far-field scattering for linear antenna arrays with identical, uniformly spaced elements.

Computer generation

Computer generation of a zero mean MCN vector for a specified covariance matrix $\mathbf{R}$ is performed by generating a vector $\mathbf{a}$ of i.i.d. complex normal elements with unit variance. The transformation

$$\mathbf{y} = \mathbf{\Sigma}\ \mathbf{\Lambda}^{1/2}\ \mathbf{a} \tag{1.31}$$

produces a new complex normal vector with the proper covariance, where $\mathbf{\Sigma}$ and $\mathbf{\Lambda}$ are the matrix of eigenvectors and the diagonal matrix of eigenvalues of $\mathbf{R}$, respectively.

For the case of the Kronecker model, applying this method to construct $\mathbf{H}$ results in

$$\mathbf{H} = \mathbf{R}_R^{1/2}\mathbf{H}_{\text{IID}}\mathbf{R}_T^{1/2\ T}, \tag{1.32}$$

where $\mathbf{H}_{\text{IID}}$ is an $N_R \times N_T$ matrix of i.i.d. complex normal elements.

Complex and power envelope correlation

The *complex correlation* in (1.20) is the preferred way to specify the covariance of the complex normal channel matrix. However, for cases in which only power information is available, a *power envelope correlation* may be constructed. Let $\mathbf{R}_P = \mathrm{E}\left\{(|\mathbf{h}|^2 - \boldsymbol{\mu}_P)(|\mathbf{h}|^2 - \boldsymbol{\mu}_P)^T\right\}$, where $\boldsymbol{\mu}_P = \mathrm{E}\left\{|\mathbf{h}|^2\right\}$, and $|\cdot|^2$ is an element-wise squaring of the magnitude. Interestingly, for a zero-mean MCN distribution with covariance $\mathbf{R}$, the power correlation matrix is simply $\mathbf{R}_P = |\mathbf{R}|^2$. This can be seen by considering a bivariate complex normal vector $[a_1\ a_2]^T$ with covariance matrix

$$\mathbf{R} = \begin{bmatrix} R_{11} & R_{R,12} - jR_{I,12} \\ R_{R,12} + jR_{I,12} & R_{22} \end{bmatrix}, \tag{1.33}$$

where all $R_{\{\cdot\}}$ are real scalars, and subscripts R and I correspond to real and imaginary parts, respectively. Letting $u_m = \mathrm{Re}\{a_m\}$ and $v_m = \mathrm{Im}\{a_m\}$, the complex normal distribution may also be represented by the 4-variate real Gaussian vector $[u_1\ u_2\ v_1\ v_2]^T$ with covariance matrix

$$\mathbf{R}' = \frac{1}{2}\left[\begin{array}{cc|cc} R_{11} & R_{R,12} & 0 & R_{I,12} \\ R_{R,12} & R_{22} & -R_{I,12} & 0 \\ \hline 0 & -R_{I,12} & R_{11} & R_{R,12} \\ R_{I,12} & 0 & R_{R,12} & R_{22} \end{array}\right]. \tag{1.34}$$

The power correlation of the mth and nth elements of the complex normal vector is

$$\begin{aligned} R_{P,mn} &= \mathrm{E}\left\{|a_m|^2|a_n|^2\right\} - \mathrm{E}\left\{|a_m|^2\right\}\mathrm{E}\left\{|a_n|^2\right\} \\ &= \mathrm{E}\left\{(u_m^2 + v_m^2)(u_n^2 + v_n^2)\right\} - 4\,\mathrm{E}\left\{u_m^2\right\}\mathrm{E}\left\{u_n^2\right\} \\ &= 4\mathrm{E}^2\{u_m u_n\} + 4\mathrm{E}^2\{u_m v_n\}, \end{aligned} \tag{1.35}$$

where the structure of (1.34) was used in conjunction with the identity

$$\mathrm{E}\left\{A^2B^2\right\} = \mathrm{E}\left\{A^2\right\}\mathrm{E}\left\{B^2\right\} + 2\mathrm{E}^2\{AB\}. \tag{1.36}$$

This identity is true for real zero-mean Gaussian random variables A and B and is easily derived from tabulated multidimensional normal distribution moment integrals [38]. The magnitude squared of the complex envelope correlation is

$$\begin{aligned} |R_{mn}|^2 &= |\,\mathrm{E}\{u_m u_n\} + \mathrm{E}\{v_m v_n\} + j(-\mathrm{E}\{u_m v_n\} + \mathrm{E}\{v_m u_n\})|^2 \\ &= 4\mathrm{E}^2\{u_m u_n\} + 4\mathrm{E}^2\{u_m v_n\}, \end{aligned} \tag{1.37}$$

and therefore, $\mathbf{R}_P = |\mathbf{R}|^2$. Thus, for a given power correlation $\mathbf{R}_P$, we usually have a family of compatible complex envelope correlations. For simplicity, we may let $\mathbf{R} = \sqrt{\mathbf{R}_P}$,

where $\sqrt{\cdot}$ is element-wise square root, to obtain the complex-normal covariance matrix for a specified power correlation. However, care must be taken, since $\sqrt{\mathbf{R}_P}$ is not guaranteed to be positive semi definite. Although this method is convenient, for many scenarios it can lead to very high modeling error since only power correlations are required [39].

Covariance models

Research in the area of random matrix channel modeling has proposed many possible methods for defining the covariance matrix $\mathbf{R}$. Early MIMO studies assumed an i.i.d. MCN distribution for the channel matrix ($\mathbf{R} = \mathbf{I}$) resulting in high channel capacity [40]. This model is appropriate when the multipath scattering is sufficiently rich and the spacing between antenna elements is large. However, for most realistic scenarios the i.i.d. MCN model is overly optimistic, motivating the search for more detailed specification of the covariance.

Although only approximate, closed-form expressions for covariance are most convenient for analysis. Perhaps the most obvious expression for covariance is that obtained by extending Jakes' model [18] to the multiantenna case as was performed in generating Figure 1.5. Assuming shift invariance and separability of the covariance, we may write

$$R_{mn,pq} = J_0\left(2\pi \left\|\mathbf{x}_{R,m} - \mathbf{x}_{R,p}\right\|\right) J_0\left(2\pi \left\|\mathbf{x}_{T,n} - \mathbf{x}_{T,q}\right\|\right), \tag{1.38}$$

where $\mathbf{x}_{P,m}$, $P \in \{T, R\}$ is the vectorial location of the mth transmit or receive antenna in wavelengths and $\|\cdot\|$ is the vector Euclidean norm. Alternatively, let r_T and r_R represent the real transmit and receive correlation, respectively, for signals on antennas that are immediately adjacent to each other. We can then assume the separable correlation function is exponential, or

$$R_{mn,pq} = r_R^{-|m-p|} r_T^{-|n-q|}. \tag{1.39}$$

This model builds on our intuition that correlation should decrease with increasing antenna spacing. Assuming only correlation at the receiver so that

$$R_{mn,pq} = r_R^{-|m-p|} \delta_{nq}, \tag{1.40}$$

where δ_{mp} is the Kronecker delta, bounds for channel capacity may be computed in closed form, leading to the observation that increasing r_R is effectively equivalent to decreasing SNR [41]. The exponential correlation model has also been proposed for urban measurements [5].

Other methods for computing covariance involve the use of the path-based models in Section 1.3.3 and direct measurement. When path-based models assume that the path gains, given by β_ℓ in (1.4), are described by complex normal statistics, the resulting channel matrix is MCN. Even when the statistics of the path gains are not complex normal, the statistics of the channel matrix may tend to the MCN from the central limit theorem if there are enough paths. In either case, the covariance for a specific environment may be computed directly from the known paths and antenna properties. On the other hand, direct measurement provides an exact site-specific snapshot of the covariance [42, 43, 14], assuming that movement during the measurement is sufficiently small to achieve stationary statistics. This approach potentially reduces a large set of channel matrix measurements into a smaller set

of covariance matrices. When the Kronecker assumption holds, the number of parameters may be further reduced.

Modifications have been proposed to extend the simpler models outlined above to account for dual polarization and time-variation. For example, given existing models for single-polarization channels, a new dual-polarized channel matrix can be constructed as [44]

$$\mathbf{H} = \begin{bmatrix} \mathbf{H}_{\mathrm{VV}} & \sqrt{X}\mathbf{H}_{\mathrm{VH}} \\ \sqrt{X}\mathbf{H}_{\mathrm{HV}} & \mathbf{H}_{\mathrm{HH}} \end{bmatrix}, \tag{1.41}$$

where the subchannels H_{QP} are single-polarization MIMO channels that describe propagation from polarization P to polarization Q, and X represents the ratio of the power scattered into the orthogonal polarization to the power that remains in the originally transmitted polarization. This very simple model assumes that the various single-polarization subchannels are independent, an assumption that is often true in practical scenarios. The model may also be extended to account for the case where the single-polarization subchannels are correlated [45]. Another example modification includes the effect of time variation in the i.i.d. complex normal model by writing [46]

$$\mathbf{H}^{(r+t)} = \sqrt{\alpha_t}\mathbf{H}^{(r)} + \sqrt{1-\alpha_t}\mathbf{W}^{(r+t)}, \tag{1.42}$$

where $\mathbf{H}^{(t)}$ is the channel matrix at the tth time step, $\mathbf{W}^{(t)}$ is an i.i.d. MCN-distributed matrix at each time step, and α_t is a real number between 0 and 1 that controls the channel stationarity. For example, for $\alpha_t = 1$, the channel is time-invariant, and for $\alpha_t = 0$, the channel is completely random.

Unconventional random matrix models

Although most random matrix models have focused on the MCN distribution for the elements of the channel matrix, here we highlight two interesting exceptions. In order to describe rank-deficient channels with low transmit/receive correlation (i.e., the *keyhole* or *pinhole* channel [47]), random channel matrices of the form [48]

$$\mathbf{H} = \mathbf{R}_R^{1/2}\mathbf{H}_{\mathrm{IID},1}\mathbf{R}_S^{1/2}\mathbf{H}_{\mathrm{IID},2}\mathbf{R}_T^{1/2\ T} \tag{1.43}$$

have been proposed, where $\mathbf{R}_T$ and $\mathbf{R}_R$ represent the separable transmit and receive covariances present in the Kronecker model, $\mathbf{H}_{\mathrm{IID},1}$ and $\mathbf{H}_{\mathrm{IID},2}$ are $N_R \times S$ and $S \times N_T$ matrices containing i.i.d. complex normal elements, $\mathbf{R}_S$ is the so-called scatterer correlation matrix, and the dimensionality S corresponds roughly to the number of scatterers. Although heuristic in nature, this model has the advantage of separating local correlation at the transmit and receive and global correlation because of long-range scattering mechanisms, thus allowing adequate modeling of rank-deficient channels.

Another very interesting random matrix modeling approach involves allowing the number of transmit and receive antennas as well as the scatterers to become infinite, while setting finite ratios for transmit to receive antennas and transmit antennas to scatterers [42, 49]. Under certain simplifying assumptions, closed-form expressions may be obtained for the singular values of the channel matrix as the matrix dimension tends to infinity. Therefore, for systems with many antennas, this model provides insight into the overall behavior of the eigenmodes for MIMO systems.

1.3.2 Geometric discrete scattering models

By appealing more directly to the environment propagation physics, we can obtain channel models that provide MIMO performance estimates which closely match measured observations. Typically, this is accomplished by determining the AOD, AOA, TOA (generally used only for frequency selective analyses), and complex channel gain (attenuation and phase shift) of the electromagnetic plane waves linking the transmit and receive antennas. Once these propagation parameters are determined, the transfer matrix can be constructed using (1.4).

Perhaps the simplest models based on this concept place scatterers within the propagation environment, assigning a complex electromagnetic scattering cross-section to each one. The cross-section is generally assigned randomly on the basis of predetermined statistical distributions. The scatterer placement can also be assigned randomly, although often some deterministic structure is used in scatterer placement in an effort to match a specific type of propagation environment or even to represent site-specific obstacles. Simple geometrical optics is then used to track the propagation of the waves through the environment, and the time/space parameters are recorded for each path for use in constructing the transfer matrix. Except in the case of the two-ring model discussed below, it is common to only consider waves that reflect from a single scatterer (single bounce models).

One commonly used discrete scattering model is based on the assumption that scatterers surrounding the transmitter and receiver control the AOD and AOA respectively. Therefore, two circular rings are "drawn" with centers at the transmit and receive locations and whose radii represent the average distance between each communication node and their respective scatterers. The scatterers are then placed randomly on these rings. Comparison with experimental measurements has revealed that when determining the propagation of a wave through this simulated environment, each transmit and receive scatterer participates in the propagation of only one wave (transmit and receive scatterers are randomly paired). The scenario is depicted in Figure 1.8. These *two-ring* models are very simple to generate and provide flexibility in modeling different environments through adaptation of the scattering ring radii and scatterer distributions along the ring. For example, in something like a forested environment the scatterers might be placed according to a uniform distribution in angle around the ring. In contrast, in an indoor environment a few groups of closely spaced scatterers might be used to mimic the "clustered" multipath behavior frequently observed.

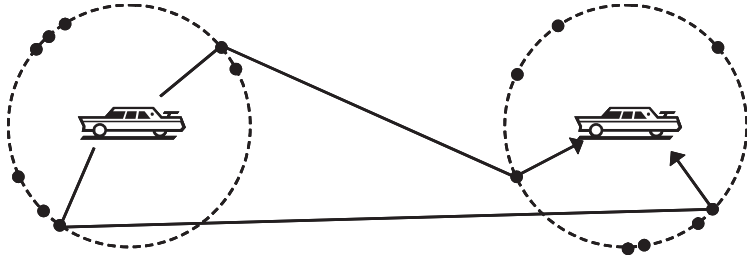

Figure 1.8 Geometry of a typical two-ring discrete scattering model showing some representative scattering paths.

Another practical method for choosing scatterer placement is to draw a set of ellipses with varying focal lengths whose foci correspond to the transmit and receive positions. Scatterers are then placed according to a predetermined scheme on these ellipses, and only single reflections are considered. In this model, all waves bouncing off scatterers located on the same ellipse will have the same propagation time delay, leading to the designation of *constant delay ellipses*. The spacing of the ellipses should be determined according to the arrival time resolution desired from the model, which would typically correspond to the inverse of the frequency bandwidth of the communication signal. With the spacing so determined, the number of rings should be chosen to provide the proper average delay spread associated with the propagation environment of interest.

In addition to their relative simplicity, these models have two interesting features. First, once the scattering environment has been realized using an appropriate mechanism, one or both of the communication nodes can move within the environment to simulate mobility. Second, with certain statistical scatterer distributions, convenient, closed-form statistical distributions can be found for delay spread, angular spread, and spatial correlation [50–52].

1.3.3 Statistical cluster models

Statistical cluster models directly specify distributions on the multipath AOD/AOA, TOA, and complex amplitude. Most current models are based on initial work by Turin, *et al.* [53] who observed that multipath components can be grouped into clusters that decay exponentially with increasing delay time. Intuitively, a single cluster of arrivals might correspond to a single scattering object and the arrivals within the cluster arise because of smaller object features. Later work applied the model to indoor scenarios [54] and added directional information [44, 22, 55, 56]. Statistical descriptions of the multipath arrival parameters can be obtained from measurements or from ray-tracing simulations [57]. Provided that the underlying statistical distributions are properly specified, these models can offer highly accurate channel representations (in a statistical sense). As a result, in this section we will detail one implementation of such a model that extends the well-known Saleh-Valenzuela model of [54] to include AOA/AOD in addition to TOA and multipath amplitude. This model will be referred to as the *Saleh-Valenzuela Model with Angle* or simply *SVA model*.

The SVA model is based on the experimentally observed phenomenon that multipath arrivals appear at the receiver in clusters in both space and time. We will refer to arrivals within a cluster as *rays*, and will restrict our discussion to the horizontal plane for simplicity ($\theta_T = \theta_R = \pi/2$). If we assume we have L clusters with K rays per cluster, then the directional channel impulse response of (1.2) can be written as

$$h_P(\tau, \phi_R, \phi_T) = \frac{1}{\sqrt{LK}} \sum_{\ell=0}^{L-1} \sum_{k=0}^{K-1} \beta_{k\ell} \delta(\tau - T_\ell - \tau_{k\ell}) \times \delta(\phi_T - \Phi_{T,\ell} - \phi_{T,k\ell}) \delta(\phi_R - \Phi_{R,\ell} - \phi_{R,k\ell}) \tag{1.44}$$

where we have removed the time dependence, and the summation now explicitly reveals the concept of clusters (index ℓ) and rays within the cluster (index k). The parameters T_ℓ, $\Phi_{T,\ell}$, and $\Phi_{R,\ell}$ represent the initial arrival time, mean departure angle, and mean arrival angle, respectively, of the ℓth cluster. Also, in this context, the kth ray arrival time $\tau_{k\ell}$, departure

angle $\phi_{T,k\ell}$, and arrival angle $\phi_{R,k\ell}$ are taken with respect to the mean time/angle values for the ℓth cluster.

It is conventional to specify the cluster and ray parameters as random variables that obey a predefined statistical distribution. We must first identify the times of arrivals of the multipath components. One common description defines the PDF of the cluster arrival time T_ℓ conditioned on the value of the prior cluster arrival time as

$$p\left(T_\ell | T_{\ell-1}\right) = \Lambda_T e^{-\Lambda_T (T_\ell - T_{\ell-1})},\ T_\ell > T_{\ell-1},\ T_0 > 0 \tag{1.45}$$

where Λ_T is a parameter that controls the cluster arrival rate for the environment of interest. Similarly, the arrival time for the kth ray in the ℓth cluster obeys the conditional PDF

$$p\left(\tau_{k\ell} | \tau_{k-1,\ell}\right) = \lambda_\tau e^{-\lambda_\tau (\tau_{k\ell} - \tau_{k-1,\ell})},\ \tau_{k\ell} > \tau_{k-1,\ell},\ \tau_{0\ell} > 0 \tag{1.46}$$

where λ_τ controls the ray arrival rate.

With the arrival times defined, we focus on the complex gain $\beta_{k\ell}$. This gain has a magnitude that is Rayleigh distributed, with the expected power (or variance) satisfying

$$\mathrm{E}\left\{|\beta_{k\ell}|^2\right\} = \mathrm{E}\left\{|\beta_{00}|^2\right\} e^{-T_\ell / \Gamma_T} e^{-\tau_{k\ell}/\gamma_\tau}, \tag{1.47}$$

which makes the amplitudes of the clusters as well as the amplitudes of the rays within the clusters decay exponentially with the time constants Γ_T and γ_τ, respectively. The phase of the complex gain is assumed uniformly distributed on $[0, 2\pi]$.

Finally, the angles of departure and arrival must be specified. For indoor and dense urban areas where scattering tends to come from all directions, the cluster departure and arrival angles can be modeled as uniformly distributed random variables on $[0, 2\pi]$. On the basis of measured data taken in [22], a two-sided Laplacian distribution is assumed for the ray AOA/AOD distribution with PDF given by

$$p(\phi_P) = \frac{1}{\sqrt{2}\sigma_{P,\phi}} \exp\left(-\left|\sqrt{2}\phi_P / \sigma_{P,\phi}\right|\right) \tag{1.48}$$

where $P \in \{T, R\}$ and $\sigma_{P,\phi}$ is the standard deviation of angle in radians. Other distributions, such as a simple Gaussian, can also be used to describe this parameter.

When using the model for narrowband implementation (the maximum multipath delay is much shorter than a symbol duration), the system cannot temporally resolve all of the arrivals within each cluster. The rays within a cluster all appear to arrive at the same time, and therefore we can simplify the model by letting the average ray power in each cluster remain constant rather than decaying exponentially. This implies that λ_τ and γ_τ are not important for model implementation. Similarly, we can arbitrarily set $\Lambda_T = 1$, since the narrowband assumption already specifies that the system cannot resolve the clusters temporally, making the absolute value of T_ℓ unimportant. Under this narrowband approximation, we will use the terminology SVA(Γ_T, σ_ϕ) to denote the SVA model with constant average ray power and unit cluster arrival rate and where $\sigma_\phi = \sigma_{R,\phi} = \sigma_{T,\phi}$.

With all of the parameters and distributions of the SVA model specified, a statistical realization of a propagation channel can be generated. The transfer matrix for this channel realization may then be constructed directly by computing (1.4) for the antennas of interest. When statistics of the channel behavior are desired, an ensemble of realizations must be created and a new channel matrix created for each realization. Statistics can then be constructed concerning the transfer matrix (matrix element distributions, spatial

correlation) or concerning the performance of the MIMO system using the transfer matrix (capacity).

Comparison of model and data

In [22], high-resolution AOA measurements were performed on the same floor of the same building the transfer matrix measurements summarized in Section 1.2.2 were taken. Although the AOA measurements were at a higher frequency (≈7 GHz), the extracted parameters serve as a logical starting point. The key parameters discovered during that study are $\sigma_\phi = 26^\circ$, $\Gamma_T = 2$, $\Lambda_T = 1$. For simulation, transmit and receive cluster arrival angles are assumed to be uniform on $[0, 2\pi]$ radians. The data below is compared to two measured data sets: (i) the data from a 4×4 system using vertically polarized patch antennas with $\lambda/2$ element separation, and (ii) the data from set 10×10-V discussed in Section 1.2. For the monopole array used in the 10×10 measurements, the radiation pattern of the mth monopole is specified as

$$e_{P,m}(\phi_P) = \exp\{jk_0(x_{P,m}\cos\phi_P + y_{P,m}\sin\phi_P)\}, \tag{1.49}$$

where $P \in \{T, R\}$, $k_0 = 2\pi/\lambda$ is the free-space wavenumber, and $(x_{P,m}, y_{P,m})$ is the location of the mth antenna referenced to the appropriate array coordinate frame. For the patch array used in the 4×4 measurements, the radiation patterns were obtained using an electromagnetic solver. In all model simulations, 10^5 channels are used (100 cluster configurations with 1000 channels each).

Figure 1.9 compares CCDFs of capacity (obtained using the water-filling algorithm) for channel matrices obtained by measurement and by Monte Carlo simulations of the SVA model. The fit between the measured and modeled channels is very good, implying that the SVA model is able to capture the important mechanisms that contribute to the channel capacity. Additional work has shown that the SVA model not only captures the capacity behavior but also accurately models pairwise joint statistics of the channel transfer matrix [44]. These results suggest that from a statistical perspective, models such as the SVA model detailed here can accurately represent physical propagation channels.

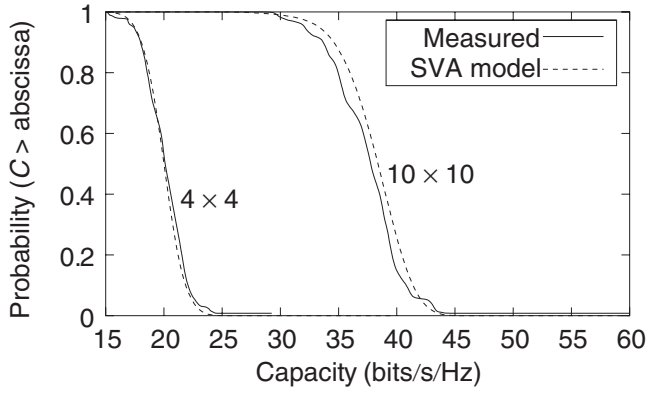

Figure 1.9 Comparison of capacity CCDFs for measured data and SVA model simulations for 4×4 and 10×10 MIMO systems.

Comparison with random matrix models

Figure 1.10 plots capacity CCDFs for channel matrices obtained from the SVA model with parameters $\Gamma_T = 2$, $\sigma_\phi = 26^\circ$, and uniform cluster AOA/AOD. Results for matrices drawn from the MCN with the covariance **R** computed directly from the measured data are also shown. Both sets of data use linear arrays of monopoles, with the 4×4 and 8×8 configurations using antenna element spacings of $\lambda/2$ and $\lambda/4$, respectively.

For the 4×4 results, use of the complex correlation provides a somewhat optimistic estimate of the capacity, while the power correlation works surprisingly well, given that this approach neglects phase information in the covariance. However, for the 8×8 channels, the addition of antennas and reduction in antenna spacing amplifies the deficiencies associated with the random matrix models, leading to significant discrepancies in the results produced by both techniques. In particular, neglecting phase information by using the power correlation technique creates significant error in the results.

Other model considerations

A variety of other extensions to statistical path-based models such as the SVA model outlined here are possible. For example, the SVA model as presented above is valid only for a single polarization. For dual polarizations, it has been found that generating a different SVA model realization for each different polarization works effectively [44]. Also, if movement of one of the nodes is to be considered, the path configuration should evolve. This is commonly handled through statistically determining "death" of clusters and "birth" of new ones [57]. Finally, some studies have used cluster models to describe the impact of distant scatterers with discrete scattering models to represent the effect of local scatterers [58, 59].

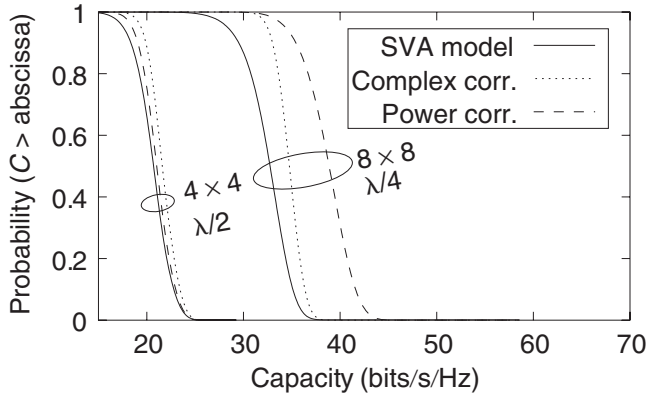

Figure 1.10 Capacity CCDFs for the 4×4 channels with $\lambda/2$ interelement spacing and 8×8 channels with $\lambda/4$ interelement spacing. Results are shown for the SVA model and MCN model with complex and power covariances obtained directly from experimental observations.

1.3.4 Deterministic ray tracing

Deterministic site-specific modeling begins by creating a two- or three-dimensional computer model of a propagation environment. The response of the model to electromagnetic excitation may then be obtained through computational techniques. Such models can also provide statistical channel information by applying Monte Carlo analysis on many random transmit/receive locations and/or model geometries.

Ray tracing [60–64] has emerged as the most popular technique for the analysis of site-specific scenarios, due to its ability to analyze very large structures with reasonable computational resources. The technique is based on geometrical optics, often supplemented by diffraction theory to enhance accuracy in shadowed regions. Recent studies have further combined ray tracing with full-wave electromagnetic solvers to model objects with features that are comparable to the illumination wavelength [65, 66].

Ray-tracing techniques have demonstrated reasonable accuracy in predicting large-scale path loss variation, with error standard deviations of 3–7 dB being reported. However, preliminary comparisons of ray-tracing predictions with measurements indicate that the simulations tend to underestimate MIMO channel capacity [67], likely due more to oversimplification of the geometrical scenario representation than failure of the electromagnetic simulation approach. Other recent work [68] shows promising agreement in AOAs of measured and simulated microcells. In this case, the results can be combined with a random distribution for phase [68–71] to create a complete model. Further work is needed to identify how much model detail is required to correctly represent the channel.

Ray-tracing simulations have been used to study MIMO channel characteristics such as spatial-signature variation with small-scale movement [72], capacity variation with array location and antenna spacing [73, 74], and angular clustering of multipath arrivals [75]. Ray-tracing studies have also led to the development of simpler statistical models such as those described in Section 1.3.3.

1.4 The Impact of Antennas on MIMO Performance

The propagation environment plays a dominant role in determining the capacity of the MIMO channel. However, robust MIMO performance depends also on proper implementation of the antenna system. To see this, consider two receive antennas with vector field patterns $\mathbf{e}_1(\theta, \phi)$ and $\mathbf{e}_2(\theta, \phi)$ and placed at the coordinates $(-d/2, 0, 0)$ and $(d/2, 0, 0)$ in Cartesian space. A set of L plane waves, with the ℓth plane wave characterized by complex strength E_ℓ, arrival angles (θ_ℓ, ϕ_ℓ), and electric field polarization $\hat{e}_\ell$, impinges on the antenna array. The signals received by the two antennas are given as

$$s_1 = \sum_{\ell=1}^{L} E_\ell \left[\mathbf{e}_1(\theta_\ell, \phi_\ell) \cdot \hat{e}_\ell\right] e^{-j(\pi d/\lambda) \sin\theta_\ell \cos\phi_\ell}$$

$$s_2 = \sum_{\ell=1}^{L} E_\ell \left[\mathbf{e}_2(\theta_\ell, \phi_\ell) \cdot \hat{e}_\ell\right] e^{j(\pi d/\lambda) \sin\theta_\ell \cos\phi_\ell}, \tag{1.50}$$

where λ is the free-space wavelength. For the MIMO system to work effectively, the signals s_1 and s_2 must be unique, despite the fact that both antennas observe the same set of plane

waves, which can be accomplished when each antenna provides a unique weighting to each of the plane waves. Equation (1.50) reveals that this can occur in three different ways:

1. On the basis of the different antenna element positions, each antenna places a unique phase on each multipath component based on its arrival angles. This is traditional *spatial diversity*.

2. If the radiation patterns $\mathbf{e}_1(\theta, \phi)$ and $\mathbf{e}_2(\theta, \phi)$ are different, then each multipath will be weighted differently by the two antennas. When the antennas share the same polarization but have different magnitude and phase responses in different directions, this is traditional *angle diversity*.

3. If in case 2 the two antennas have different polarizations, the dot product will lead to a unique weighting of each multipath component. This is traditional *polarization diversity*.

It is noteworthy that both angle and polarization diversity are subsets of the more inclusive *pattern diversity*, which simply implies that the two antenna radiation patterns (magnitude, phase, and polarization) differ to create the unique multipath weighting.

Many of the measurement and modeling approaches outlined above, particularly those based on the multipath wave parameters, provide a provision for including these antenna properties into the formulation of the channel matrix. In fact, direct measurement of the channel matrix inherently includes all antenna properties, although the direct channel matrix models typically do not. This section uses some of these appropriate measurement and modeling techniques to demonstrate the performance impact of antenna properties on MIMO system performance. Such a discussion must include the impact of antenna mutual coupling both on the antenna radiation/reception properties and the power collection capabilities of the antenna when interfaced to the RF subsystem. Therefore, an extension of the modeling approaches is presented that accurately accounts for mutual coupling as well as amplifier noise on MIMO system performance.

1.4.1 Spatial diversity

It is important to emphasize that the transfer matrix $\mathbf{H}$ in (1.5) depends not only on the propagation environment but also on the array configurations. The question becomes which array topology is best in terms of maximizing capacity (perhaps in an average sense over a variety of propagation channels) or minimizing symbol error rates. This is difficult to answer definitively, since the optimal array shape depends on the site-specific propagation characteristics. One rule of thumb is to place antennas as far apart as possible to reduce the correlation between the received signals.

There has been one notable study where several different array types were explored for both the base station and the mobile unit in an outdoor environment [76]. The base station antennas included single and dual polarization array and multibeam structures. The arrays on the mobile were constructed from monopoles to achieve spatial, angle, and/or polarization diversity. All of the array configurations provided very similar performance, with the exception of the multibeam base station antennas, which resulted in a 40–50% reduction in measured capacity since generally only one of the beams pointed in the direction

of the mobile. These results suggest that average capacity is relatively insensitive to array configuration provided the signal correlation is adequately low.

1.4.2 Pattern (angle and polarization) diversity

If the radiation patterns of the antenna elements are *orthogonal* when integrated over the range of multipath arrival angles, the goal of having the antenna apply a unique weighting to the incident multipath waves is optimally achieved [77]. For now neglecting the pattern polarization, this can be accomplished with proper element design to achieve the appropriate angular distribution of field strength. For example, one suggested approach for realizing such a situation involves the use of a single multimode antenna where the patterns for different modes exhibit high orthogonality (low correlation) [78]. However, in such a case it is important to use modes that not only provide the high orthogonality required but also all properly direct their energy in angular regions where multipath power is the highest. Failure to do so can reduce the effective received signal power so severely that the benefit gained by pattern orthogonality can be outweighed by the loss in SNR due to poor excitation/reception within the environment of interest [79].

A more common application of pattern diversity is the use of antennas with different polarizations. This is an intriguing concept, since polarization allows pattern orthogonality that can increase communication capacity even when no multipath is present. Therefore, when implementing MIMO systems, use of different polarizations can enable MIMO performance to remain high even when a mobile subscriber moves into a region where the multipath richness is low. However, proper implementation of polarization diversity for MIMO systems requires understanding of the physics involved.

To begin this analysis, consider the case of infinitesimal electric and magnetic current elements (dipoles) radiating into free space. For a three-dimensional coordinate frame, we may orient each of the two current types in the $\hat{x}$, $\hat{y}$, and $\hat{z}$ directions. Each of these six possible currents will create a unique vector far-field radiation pattern given by

Current orientation	**Pattern: electric current**	**Pattern: magnetic current**
$\hat{x}$	$\mathbf{e}_1 = -\hat{\theta}\cos\theta\cos\phi + \hat{\phi}\sin\phi$	$\mathbf{e}_4 = \hat{\theta}\sin\phi + \hat{\phi}\cos\theta\cos\phi$
$\hat{y}$	$\mathbf{e}_2 = -\hat{\theta}\cos\theta\sin\phi - \hat{\phi}\cos\phi$	$\mathbf{e}_5 = -\hat{\theta}\cos\phi + \hat{\phi}\cos\theta\sin\phi$
$\hat{z}$	$\mathbf{e}_3 = \hat{\theta}\sin\theta$	$\mathbf{e}_6 = -\hat{\phi}\sin\theta$

These results make it very clear that polarization diversity *cannot* be completely independent of angle diversity, since the angular distribution of power is dependent on the orientation (polarization) of the radiating current.

Now, consider all six possible infinitesimal dipoles located at the same point in space and receiving an incident multipath field. Assuming that on average, the power in the multipath field is uniformly distributed in angle over a solid angle sector $\Delta\Omega = (\Delta\theta, \Delta\phi)$ and equally represents both polarizations, we can express the elements of the covariance matrix of the signals received by the six antennas as [80]

$$R_{pq} = \int_{\Delta\Omega} \mathbf{e}_p(\Omega) \cdot \mathbf{e}_q^*(\Omega)\, d\Omega. \tag{1.51}$$

We then define the eigenvalues of the matrix $\mathbf{R}$ as $\hat{\lambda}_p$, $1 \leq p \leq 6$. If all eigenvalues are equal and nonzero, this implies that six spatial degrees of freedom are created by the antenna

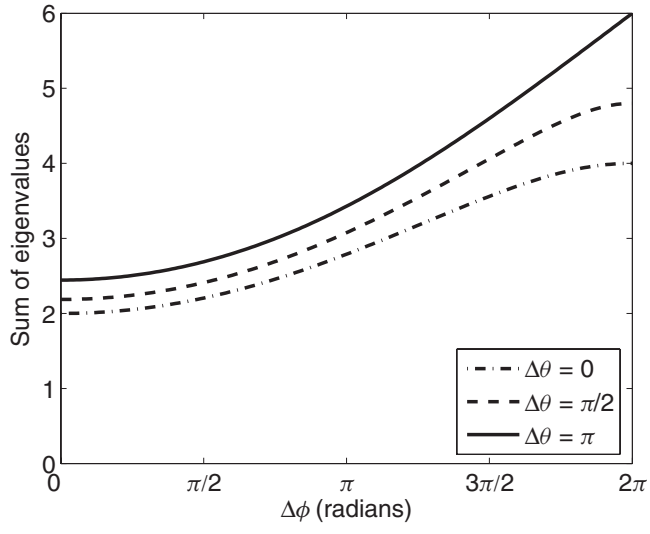

Figure 1.11 Normalized sum of the eigenvalues of the correlation matrix versus incident field angle spread parameters assuming ideal point sensors.

structure. From a MIMO perspective, this would mean the creation of six independent spatial communication channels. To assess this number of communication channels, we will use the parameter

$$\kappa = \frac{1}{\hat{\lambda}_{\max}} \sum_{p=1}^{6} \hat{\lambda}_p, \tag{1.52}$$

where $\hat{\lambda}_{\max}$ represents the maximum eigenvalue. The quantity κ can assume values in the range $1 \leq \kappa \leq 6$, and gives some indication of the number of spatial degrees of freedom available in the channel.

Figure 1.11 plots κ versus angular spread parameter $\Delta\phi$ for three different values of $\Delta\theta$. As can be seen, for a single propagation path ($\Delta\theta = \Delta\phi = 0$), only two channels exist corresponding to the two possible polarizations of the incident plane wave. As the angle spread increases, κ increases to a maximum value of six, indicating the availability of six independent communication modes [81]. Because observed elevation spread in indoor and urban environments is relatively small, the curve for $\Delta\theta = 0$ is particularly interesting. Most noteworthy for this case is the fact that if full azimuthal spread is considered, the correlation matrix becomes diagonal, indicating six independent channels. These channels, however, are not all equally "good" since the power received by the $\hat{z}$ oriented sensors is twice as large as the power received by the other sensors [18].

From a practical standpoint, constructing a multipolarized antenna that can achieve the performance suggested in Figure 1.11 is problematic. Using half-wavelength dipoles and full-wavelength loops leads to strong mutual coupling and nonideal pattern characteristics that can reduce the number of independent channels. One interesting geometry is a cube consisting of dipole antennas to obtain a high degree of polarization diversity in a compact

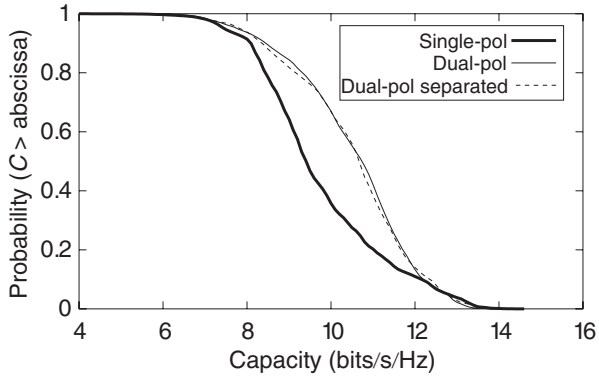

Figure 1.12 CCDFs for 2×2 channels employing different types of polarization/spatial separation with realistic normalization.

form [82]. It is, however, much more common to simply construct antennas with two polarizations and use a combination of polarization and spatial diversity to achieve MIMO capacity. The linear patch arrays employed in the measurements outlined in Section 1.2 consist of four dual-polarization elements separated by a half-wavelength, and therefore allow some assessment of the performance achievable with practical geometries. In this study, four transmit/receive channels (set 4×4-VH) were used to excite both vertical and horizontal polarizations on two $\lambda/2$ separated patches on each side of the link. By looking at the appropriate submatrices of $\mathbf{H}$, the capacity can be compared for three different 2×2 subchannels: (i) Two elements with the same polarization (vertical or horizontal) but separated by $\lambda/2$, (ii) Two elements that have orthogonal polarization and are co-located, and (iii) Two elements that have both orthogonal polarization and are separated by $\lambda/2$.

When considering the effect of polarization, it is important to keep in mind that if the vertical polarization is transmitted, the received power in the horizontal polarization will typically be 3–10 dB lower than the power received in the horizontal polarization. A similar statement can be made for transmission of the horizontal polarization. This suggests that entries in the channel matrix corresponding to reception on a different polarization than the transmission will tend to be weaker than those entries corresponding to transmission and reception on the same polarization. When normalizing the channel matrix, therefore, the normalization constant is set to achieve an average SISO SNR of 20 dB for the copolarized matrix elements only. Figure 1.12 depicts the CCDFs resulting from the measured data. As can be seen, using polarization diversity tends to increase capacity over what is possible using spatial separation alone. It is also interesting that combining spatial separation and polarization does not increase the capacity over what is possible with polarization alone for this scenario.

1.4.3 Mutual coupling and receiver network modeling

In many compact devices, the antenna elements must be closely spaced, and the resulting antenna mutual coupling can impact communication performance. Evaluating the effect of

this coupling is often approached by examining how the altered radiation patterns change the signal correlation [77] and using this correlation to derive the system capacity [83–85]. When applying this technique, however, it is important to understand that there are two different physical phenomena that impact these radiation patterns:

1. When an open-circuited (coupled) antenna is placed near an antenna connected to a generator, the electromagnetic boundary conditions are changed, leading to a change in the radiation behavior. However, because the coupled antenna is open-circuited, the impact on the pattern of the driven element is often relatively minor for most practical configurations.

2. The open-circuit voltage V_c induced at the coupled antenna terminals is related to the current I_d in the driven element according to $V_c = Z_m I_d$, where Z_m is the mutual impedance. If the coupled antenna is now terminated with a load, the induced voltage will create a current in the coupled antenna that depends on the termination impedance. Therefore, the effective radiation pattern will be the superposition of the driven element pattern and the coupled element pattern weighted by this induced current. The composite pattern therefore depends on the load attached to the coupled element.

Item 2 makes it clear that ambiguity exists in defining the pattern to use in standard correlation analysis. Furthermore, since the composite pattern is a linear combination of the individual element patterns, compensation for the impact of this effect can theoretically be achieved through proper signal combination after reception, and therefore any analysis conducted in this manner only represents the performance achievable for the specific load configuration used in the computations. In this section, we present an extension to the channel modeling approaches discussed in this chapter that rigorously incorporates the electromagnetic coupling and accurately models the receiver subsystem in terms of impedance characteristics and thermal noise properties.

MIMO network model

Figure 1.13 shows a block diagram of the system model, which includes all major channel components between the coupled transmit antennas and terminated receive amplifiers, used in this analysis. We use scattering parameters (S-parameters) referenced to a real impedance Z_0 [86] to describe the network signal flow wherein the forward and reverse traveling waves are denoted as $\mathbf{a}$ and $\mathbf{b}$, respectively. The various specific traveling wave vectors, S-parameter matrices (symbol $\mathbf{S}$), and reflection coefficient matrices (symbol $\mathbf{\Gamma}$) appearing in Figure 1.13 will be identified in the following derivation.

The signal $\mathbf{a}_T$ excites the transmit array consisting of N_T mutually coupled antenna elements characterized by an S-matrix $\mathbf{S}_{TT}$. The net power flowing into the network is $\|\mathbf{a}_T\|^2 - \|\mathbf{b}_T\|^2$, which, for lossless antennas, equals the instantaneous radiated transmit power P_T^{inst}. Since $\mathbf{b}_T = \mathbf{S}_{TT}\ \mathbf{a}_T$, we have

$$P_T^{\text{inst}} = \mathbf{a}_T^H \underbrace{(\mathbf{I} - \mathbf{S}_{TT}^H \mathbf{S}_{TT})}_{\mathbf{A}} \mathbf{a}_T. \tag{1.53}$$

For zero mean signals, the average radiated power is given by

$$P_T = \mathrm{E}\left\{P_T^{\text{inst}}\right\} = \mathrm{Tr}(\mathbf{R}_a \mathbf{A}), \tag{1.54}$$

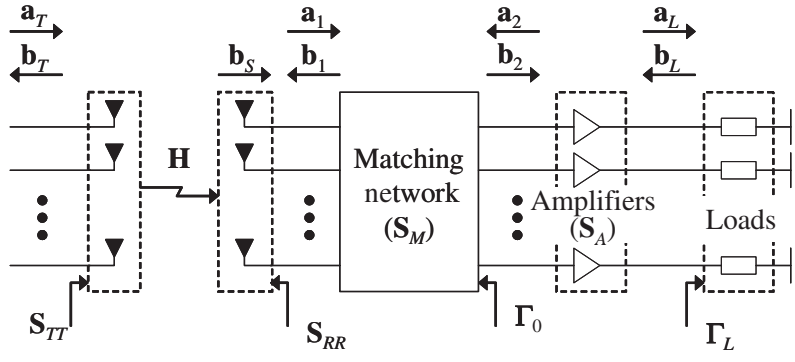

Figure 1.13 Block diagram of the MIMO system of Subsection 1.4.3 including mutually coupled arrays, propagation channel, matching network, receiver amplifiers, and loads.

where $\mathbf{R}_a = \mathrm{E}\left\{\mathbf{a}_T\ \mathbf{a}_T^H\right\}$. We emphasize that in traditional analysis of MIMO systems, the total power is taken as $\mathrm{Tr}(\mathbf{R}_a)$. Eq. (1.54) therefore illustrates one way in which antenna coupling impacts the system analysis.

The radiation pattern for the qth element of the transmit array for a unit driving current and all other elements in the array terminated in an open circuit is denoted as $\mathbf{e}_{T,q}(\theta_T, \phi_T)$, where (θ_T, ϕ_T) represent the angular spherical coordinates referenced to the transmit array origin. The two elements of the column vector represent the $\hat{\theta}$ and $\hat{\phi}$ polarizations. The total transmitted field is then

$$\mathbf{e}_T(\theta_T, \phi_T) = \sum_{q=1}^{N_T} \mathbf{e}_{T,q}(\theta_T, \phi_T)\ i_{T,q} = \mathbf{E}_T(\theta_T, \phi_T)\mathbf{i}_T, \tag{1.55}$$

where $i_{T,q}$, the qth element of $\mathbf{i}_T$, is the excitation current on the qth antenna and $\mathbf{e}_{T,q}(\theta_T, \phi_T)$ is the qth column of the $2 \times N_T$ matrix $\mathbf{E}_T(\theta_T, \phi_T)$.

We now represent the radiation pattern of the pth coupled receive element ($1 \le p \le N_R$) referenced to the receiver coordinate origin as $\mathbf{e}_{R,p}(\theta_R, \phi_R)$. Using a path-based propagation model, the open circuit voltage on the pth receive element is (see (1.4))

$$v_{R,p} = \sum_{q=1}^{N_T} \underbrace{\sum_{\ell=1}^{L} \mathbf{e}_{R,p}^T(\theta_{R,\ell}, \phi_{R,\ell})\beta_\ell\ \mathbf{e}_{T,q}(\theta_{T,\ell}, \phi_{T,\ell})}_{2Z_0 H_{P,pq}}\ i_{T,q}, \tag{1.56}$$

where the term $2Z_0$ is isolated for later convenience. The vector of received open-circuit voltages at the antenna terminals is then

$$\mathbf{v}_R = 2Z_0\mathbf{H}_P\ \mathbf{i}_T. \tag{1.57}$$

We emphasize that $\mathbf{H}_P$ represents the channel matrix derived from the physical channel impulse response as discussed in several sections of this chapter. The analysis that follows demonstrates how this model can be extended to include other effects present in the electronic subsystems.

The signal $\mathbf{b}_S$ represents the traveling wave delivered by the receive antenna terminals to a set of independent loads of resistance Z_0 (so that $\mathbf{b}_1 = \mathbf{0}$). If a general termination is attached to the array, the composite array output signal is

$$\mathbf{a}_1 = \mathbf{b}_S + \mathbf{S}_{RR}\mathbf{b}_1. \tag{1.58}$$

For an open-circuit termination ($\mathbf{a}_1 = \mathbf{b}_1$), this becomes $\mathbf{b}_S = (\mathbf{I} - \mathbf{S}_{RR})\mathbf{a}_1$. We can also express the voltage at the open-circuit antenna terminals using $\mathbf{v}_R = Z_0^{1/2}(\mathbf{a}_1 + \mathbf{b}_1) = 2Z_0^{1/2}\mathbf{a}_1$. Using these results in (1.57) and recognizing that the transmit current is $\mathbf{i}_T = Z_0^{-1/2}(\mathbf{a}_T - \mathbf{b}_T) = Z_0^{-1/2}(\mathbf{I} - \mathbf{S}_{TT})\mathbf{a}_T$, we obtain

$$\mathbf{b}_s = \underbrace{(\mathbf{I} - \mathbf{S}_{RR})\,\mathbf{H}_P\,(\mathbf{I} - \mathbf{S}_{TT})}_{\mathbf{S}_{RT}}\,\mathbf{a}_T. \tag{1.59}$$

The multiport matching network is described by the block S-parameter matrix

$$\mathbf{S}_M = \begin{bmatrix} \mathbf{S}_{11} & \mathbf{S}_{12} \\ \mathbf{S}_{21} & \mathbf{S}_{22} \end{bmatrix}, \tag{1.60}$$

where 1 and 2 refer to input and output ports, respectively. With this notation, network analysis shows that the signal $\mathbf{b}_2$ at the matching network output is

$$\mathbf{b}_2 = \mathbf{S}_{21}\,(\mathbf{I} - \mathbf{S}_{RR}\mathbf{S}_{11})^{-1}\,\mathbf{b}_S + \underbrace{\left[\mathbf{S}_{22} + \mathbf{S}_{21}\,(\mathbf{I} - \mathbf{S}_{RR}\mathbf{S}_{11})^{-1}\,\mathbf{S}_{RR}\mathbf{S}_{12}\right]}_{\boldsymbol{\Gamma}_0}\mathbf{a}_2 \tag{1.61}$$

where $\boldsymbol{\Gamma}_0$ represents the reflection coefficient at the matching network output as shown in Figure 1.13.

The pth noisy amplifier injects forward and reverse traveling noise waves $a_{\eta,p}$ and $b_{\eta,p}$, respectively, at the amplifier input. The amplifier signal-plus-noise output waves are of the form [87]

$$\mathbf{a}_2 = \mathbf{S}_{A,11}\mathbf{b}_2 + \mathbf{S}_{A,12}\mathbf{b}_L - \mathbf{S}_{A,11}\mathbf{a}_\eta + \mathbf{b}_\eta \tag{1.62}$$

$$\mathbf{a}_L = \mathbf{S}_{A,21}\mathbf{b}_2 + \mathbf{S}_{A,22}\mathbf{b}_L - \mathbf{S}_{A,21}\mathbf{a}_\eta, \tag{1.63}$$

where the subscript 'A' denotes the S-parameters of the amplifiers. Using additional network analysis with these expressions and (1.61) leads to the vector of voltages across the amplifier terminations (characterized by the reflection coefficient matrix $\boldsymbol{\Gamma}_L$) given by

$$\mathbf{v}_L = \mathbf{Q}\left[\mathbf{G}\mathbf{S}_{RT}\,\mathbf{a}_T + \boldsymbol{\Gamma}_0\,\mathbf{b}_\eta - \mathbf{a}_\eta\right]. \tag{1.64}$$

where

$$\mathbf{G} = \mathbf{S}_{21}(\mathbf{I} - \mathbf{S}_{RR}\mathbf{S}_{11})^{-1} \tag{1.65}$$

$$\mathbf{Q} = Z_0^{1/2}\,(\mathbf{I} + \boldsymbol{\Gamma}_L)\left[\left(\mathbf{I} - \boldsymbol{\Gamma}_0\mathbf{S}_{A,11}\right)\mathbf{S}_{A,21}^{-1}\left(\mathbf{I} - \mathbf{S}_{A,22}\boldsymbol{\Gamma}_L\right) - \boldsymbol{\Gamma}_0\mathbf{S}_{A,12}\boldsymbol{\Gamma}_L\right]^{-1}. \tag{1.66}$$

Matching network specification

Practical amplifier design involves specifying an amplifier performance goal and synthesizing the source and load terminations that achieve this goal. Signal amplifiers are typically designed to provide minimum noise figure, optimal power gain, or some compromise between the two [88]. Our task is to define a desired value of $\mathbf{\Gamma}_0$, which is the source termination seen by the amplifier, and use this value to determine the $\mathbf{S}_M$ for the matching network.

If the matching network is constrained to be lossless, the problem of determining $\mathbf{S}_M$ for a given $\mathbf{\Gamma}_0$ can be solved. Let $\mathbf{\Gamma}_0 = \mathbf{U}_0 \mathbf{\Lambda}_0^{1/2} \mathbf{V}_0^H$ represent the singular value decomposition (SVD) of $\mathbf{\Gamma}_0$, where $\mathbf{U}_0$ and $\mathbf{V}_0$ are unitary matrices of singular vectors and $\mathbf{\Lambda}_0^{1/2}$ is a diagonal matrix of real singular values. Similarly, let $\mathbf{S}_{RR} = \mathbf{U}_{RR} \mathbf{\Lambda}_{RR}^{1/2} \mathbf{V}_{RR}^H$ be the SVD of $\mathbf{S}_{RR}$. The matrix $\mathbf{S}_M$ can be written using the block matrix product

$$\mathbf{S}_M = \begin{bmatrix} \mathbf{V}_{RR} & \mathbf{0} \\ \mathbf{0} & \mathbf{U}_0 \end{bmatrix} \begin{bmatrix} \mathbf{\Lambda}_{11}^{1/2} & j\,(\mathbf{I} - \mathbf{\Lambda}_{11})^{1/2} \\ j\,(\mathbf{I} - \mathbf{\Lambda}_{11})^{1/2} & \mathbf{\Lambda}_{11}^{1/2} \end{bmatrix} \begin{bmatrix} \mathbf{U}_{RR} & \mathbf{0} \\ \mathbf{0} & \mathbf{V}_0 \end{bmatrix}^H. \tag{1.67}$$

We assume uncoupled amplifiers ($\mathbf{S}_{A,ij}$ and $\mathbf{\Gamma}_L$ are diagonal), so that typical design goals are achieved for diagonal $\mathbf{\Gamma}_0$. If Γ_{opt} and Γ_{MS} represent the (scalar) source reflection coefficient for achieving amplifier minimum noise figure and maximum power gain [88], respectively, then achieving the these goals are accomplished by setting $\mathbf{\Gamma}_0 = \Gamma_{opt}\mathbf{I}$ and $\mathbf{\Gamma}_0 = \Gamma_{MS}\mathbf{I}$. Since MIMO capacity depends on SNR, we expect a design for minimum noise figure to outperform one for maximum power gain.

To achieve diagonal $\mathbf{\Gamma}_0$, the matching network must be coupled to "undo" the coupling created by the antenna, and it therefore acts as an *array combining network* as well as an impedance transforming network. This is an important observation, since the linear combination of the signals in the matching network is performed *before* injection of the noise by the amplifiers. In fact, it has been shown that if the matching network produces diagonal $\mathbf{\Gamma}_0$, the capacity of a MIMO system with mutually coupled antennas can be greater than the capacity obtained when uncoupled antennas are assumed. This observation will be reinforced by the example later in this section.

Finally, while optimal matching networks must be coupled, practically speaking it is easier to design an uncoupled network. We assume that the coupled antenna impedance can be represented using only the diagonal elements of the full impedance matrix $\mathbf{Z}_{RR}$ to obtain $\overline{\mathbf{Z}}_{RR}$ and compute a diagonal $\overline{\mathbf{S}}_{RR}$ with elements $\overline{S}_{RR,ii} = (\overline{Z}_{RR,ii} - Z_0)/(\overline{Z}_{RR,ii} + Z_0)$. This value of $\overline{\mathbf{S}}_{RR}$ is then used in place of $\mathbf{S}_{RR}$ in (1.67). However, when analyzing the performance of this *self-impedance* match, the nondiagonal form of $\mathbf{S}_{RR}$ must be used in (1.64).

Coupled system capacity

Computing the capacity for the MIMO signal relationship in (1.64) requires that we formulate the covariance of $\mathbf{v}_L$ assuming the input signal $\mathbf{a}_T$ and noise are drawn from zero-mean complex Gaussian distributions. Using the statistical properties of the noise vectors $\mathbf{a}_\eta$ and $\mathbf{b}_\eta$ [87] and assuming that the noise in each amplifier is statistically uncorrelated with that

of all other amplifiers, we can express the covariance as

$$\mathbf{R}_L = \mathrm{E}\left\{\mathbf{v}_L\mathbf{v}_L^H\right\} = \mathbf{Q}\left[\mathbf{G}\mathbf{S}_{RT}\mathbf{R}_a\mathbf{S}_{RT}^H\mathbf{G}^H + \mathbf{R}_\eta\right]\mathbf{Q}^H \tag{1.68}$$

$$\begin{aligned}\mathbf{R}_\eta &= \mathrm{E}\left\{(\boldsymbol{\Gamma}_0\mathbf{b}_\eta - \mathbf{a}_\eta)(\boldsymbol{\Gamma}_0\mathbf{b}_\eta - \mathbf{a}_\eta)^H\right\} \\ &= k_B B \underbrace{\left(T_\alpha\mathbf{I} + T_\beta\boldsymbol{\Gamma}_0\boldsymbol{\Gamma}_0^H - T_\Gamma\boldsymbol{\Gamma}_0 - T_\Gamma^*\boldsymbol{\Gamma}_0^H\right)}_{T_\alpha\mathbf{R}_{\eta o}}\end{aligned} \tag{1.69}$$

where k_B is the Boltzmann constant and B is the system noise power bandwidth. The effective noise temperatures (T_α, T_β, $T_\Gamma = T_\gamma e^{j\phi_\gamma}$), which can be determined from the amplifier noise characteristics [87], are assumed identical for all amplifiers.

The capacity for the system in (1.64) can now be determined by finding the covariance $\mathbf{R}_a$ that maximizes the mutual information expression

$$I(\mathbf{v}_L, \mathbf{a}_T) = \log_2 \frac{\det\left\{\mathbf{G}\mathbf{S}_{RT}\mathbf{R}_a\mathbf{S}_{RT}^H\mathbf{G}^H + \mathbf{R}_\eta\right\}}{\det\left\{\mathbf{R}_\eta\right\}}. \tag{1.70}$$

Computing the eigenvalue decomposition $\mathbf{R}_{\eta o} = \boldsymbol{\xi}_\eta\boldsymbol{\Lambda}_\eta\boldsymbol{\xi}_\eta^H$ where $\boldsymbol{\xi}_\eta$ is unitary, the mutual information expression becomes

$$I(\mathbf{v}_L, \mathbf{a}_T) = \log_2 \det\left\{\frac{\mathbf{Y}\mathbf{R}_T\mathbf{Y}^H}{k_B B T_\alpha} + \mathbf{I}\right\}, \tag{1.71}$$

where $\mathbf{Y} = \boldsymbol{\Lambda}_\eta^{-1/2}\boldsymbol{\xi}_\eta^H\mathbf{G}\mathbf{S}_{RT}$. The capacity results when the transmit covariance matrix $\mathbf{R}_a$ is specified according to the water-filling solution, with the total transmit power limited according to $\mathrm{Tr}(\mathbf{R}_a\mathbf{A}) \le P_T$ as derived in (1.54). Because this power constraint is a departure from the typical constraint $\mathrm{Tr}(\mathbf{R}_a) \le P_T$, the water-filling procedure must be modified, as detailed in [89, 90].

Computational example

To demonstrate application of the analysis framework and to illustrate the impact of antenna coupling and amplifier matching on MIMO system capacity, we use a model problem consisting of two half-wave dipoles at transmit and receive. The coupled dipoles, which have a wire radius of 0.01λ, are characterized using the finite-difference time-domain method [91]. We use a bipolar junction transistor that for $Z_0 = 50\ \Omega$ has noise and S-parameters

$$\begin{aligned}\mathbf{S}_{11} &= 0.552\angle 169^\circ & \mathbf{S}_{12} &= 0.049\angle 23^\circ \\ \mathbf{S}_{21} &= 1.681\angle 26^\circ & \mathbf{S}_{22} &= 0.839\angle -67^\circ \\ F_{min} &= 2.5\ \mathrm{dB} & \Gamma_{opt} &= 0.475\angle 166^\circ \\ R_n &= 3.5\ \mathrm{Ohms}, & &\end{aligned} \tag{1.72}$$

where F_{min}, Γ_{opt}, and R_n represent the minimum noise figure, optimal source termination for noise figure, and effective noise resistance respectively. These parameters are converted to the effective noise temperatures T_α, T_β, and T_Γ using standard techniques.

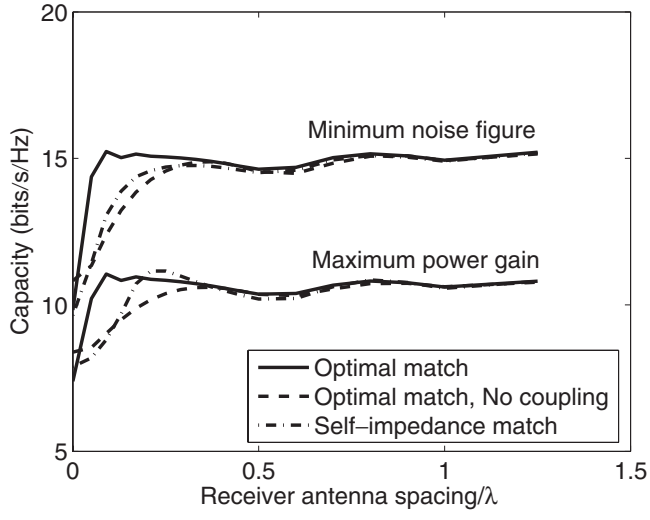

Figure 1.14 Average capacity as a function of receive dipole separation with mutual coupling (optimal and self-impedance match) as well as without mutual coupling. Matching for both minimum noise figure and maximum power gain are considered.

We use 5000 realizations of the SVA model to create a set of transfer matrices $\mathbf{H}_P$ as in (1.56). For each realization, we place single dipoles in the transmit and receive spaces and create a lossless receive matching network with $S_{11} = S_{RR}^*$ so that $\Gamma_0 = 0$ (all terms are scalars). We then can simplify the SISO SNR as

$$\text{SNR} = \frac{|S_{RT}|^2}{1 - |S_{RR}|^2} \frac{P_T}{k_B B T_\alpha}. \tag{1.73}$$

This SNR value is then averaged in space by moving each dipole in 0.1λ steps over a linear range of 1.5λ. For a given transmit power, the value of $k_B B T_\alpha$ can be computed to achieve an average SISO SNR (20 dB in this work) for the channel realization.

We next construct the matching network to achieve the specified design goal for each transmit/receive dipole spacing, as outlined in Section 1.4.3. For each configuration, we compute the capacity averaged over the 5000 channel matrices with the corresponding noise power levels $k_B B T_\alpha$. The transmit array spacing is fixed at 0.5λ for all computations.

Figure 1.14 plots the capacity as a function of receive dipole spacing for matching networks that achieve minimum noise figure and maximum amplifier gain. Results for a coupled match and a simpler self-impedance match as well as for no receiver coupling are included. We first observe that the match achieving minimum amplifier noise figure (noise figure of $F = F_{min} = 2.5$ dB) produces notably higher capacity than the match providing maximum power transfer, which generates a much higher noise figure of $F = 7.2$ dB. This result is intuitive, since ultimately capacity depends on SNR as opposed to absolute signal strength. We also observe that for close antenna spacings with high coupling, the shortcomings of the self-impedance match are evident. However, once the spacing reaches approximately $d = \lambda/4$, this match provides near optimal performance. Finally, Figure 1.14

indicates that for small antenna spacings, coupled dipoles can have a higher capacity than uncoupled ones. This possibility was discussed in Section 1.4.3.

References

[1] C. Xiao, J. Wu, S.-Y. Leong, Y. R. Zheng, and K. B. Letaief, "A discrete-time model for spatio-temporally correlated MIMO WSSUS multipath channels," in *Proc. 2003 IEEE Wireless Commun. Network. Conf.*, vol. 1, New Orleans, LA, Mar. 16-20, 2003, pp. 354–358.

[2] D. P. McNamara, M. A. Beach, P. N. Fletcher, and P. Karlsson, "Capacity variation of indoor multiple–input multiple–output channels," *Electron. Lett.*, vol. 36, pp. 2037–2038, Nov. 2000.

[3] J. W. Wallace, M. A. Jensen, A. L. Swindlehurst, and B. D. Jeffs, "Experimental characterization of the MIMO wireless channel: Data acquisition and analysis," *IEEE Trans. Wireless Commun.*, vol. 2, pp. 335–343, Mar. 2003.

[4] M. Lienard, P. Degauque, J. Baudet, and D. Degardin, "Investigation on MIMO channels in subway tunnels," *IEEE J. Sel. Areas Commun.*, vol. 21, pp. 332–339, Apr. 2003.

[5] D. Chizhik, J. Ling, P. W. Wolniansky, R. A. Valenzuela, N. Costa, and K. Huber, "Multiple-input-multiple-output measurements and modeling in Manhattan," *IEEE J. Sel. Areas Commun.*, vol. 21, pp. 321–331, Apr. 2003.

[6] C. C. Martin, J. H. Winters, H. H. Zeng, N. R. Sollenberger, and A. Dixit, "Multiple-input multiple-output (MIMO) radio channel measurements and experimental implementation for EDGE," in *Conf. Rec. 34th Asilomar Conf. Signals Syst. Comput.*, vol. 1, Pacific Grove, CA, Oct. 29 – Nov. 1, 2000, pp. 738–742.

[7] K. Yu, M. Bengtsson, B. Ottersten, D. McNamara, P. Karlsson, and M. Beach, "Second order statistics of NLOS indoor MIMO channels based on 5.2 GHz measurements," in *Proc. 2001 IEEE Glob. Telecomm. Conf.*, vol. 1, San Antonio, TX, Nov. 25-29, 2001, pp. 156–160.

[8] J. Medbo and J.-E. Berg, "Simple and accurate path loss modeling at 5 GHz in indoor environments with corridors," in *Proc. 2000 IEEE 52nd Veh. Technol. Conf.*, vol. 1, Boston, MA, Sep. 24-28, 2000, pp. 30–36.

[9] V. Erceg, P. Soma, D. S. Baum, and A. J. Paulraj, "Capacity obtained from multiple–input multiple – output channel measurements in fixed wireless environments at 2.5 GHz," in *Proc. 2002 IEEE Intl. Conf. Commun.*, vol. 1, New York, Apr. 28- May 2, 2002, pp. 396–400.

[10] M. D. Batariere, T. K. Blankenship, J. F. Kepler, T. P. Krauss, I. Lisica, S. Mukthavaram, J. W. Porter, T. A. Thomas, and F. W. Vook, "Wideband MIMO mobile impulse response measurements at 3.7 GHz," in *Proc. 2002 IEEE 55th Veh. Technol. Conf.*, vol. 1, Birmingham, AL, May 6-9, 2002, pp. 26–30.

[11] J. P. Kermoal, L. Schumacher, P. E. Mogensen, and K. I. Pedersen, "Experimental investigation of correlation properties of MIMO radio channels for indoor picocell scenarios," in *Proc. 2000 IEEE 52nd Veh. Technol. Conf.*, vol. 1, Boston, MA, Sep. 24-28, 2000, pp. 14–21.

[12] A. F. Molisch, M. Steinbauer, M. Toeltsch, E. Bonek, and R. S. Thoma, "Measurement of the capacity of MIMO systems in frequency-selective channels," in *Proc. 2001 IEEE 53rd Veh. Technol. Conf.*, vol. 1, Rhodes, Greece, May 6-9, 2001, pp. 204–208.

[13] A. F. Molisch, M. Steinbauer, M. Toeltsch, E. Bonek, and R. S. Thoma, "Capacity of MIMO systems based on measured wireless channels," *IEEE J. Sel. Areas Commun.*, vol. 20, pp. 561–569, Apr. 2002.

[14] M. Herdin, H. Özcelik, H. Hofstetter, and E. Bonek, "Variation of measured indoor MIMO capacity with receive direction and position at 5.2 GHz," *Electron. Lett.*, vol. 38, pp. 1283–1285, Oct. 10, 2002.

[15] J. Medbo and J.-E. Berg, "Spatio-temporal channel characteristics at 5 GHz in a typical office environment," in *Proc. 2001 IEEE 54th Veh. Technol. Conf.*, vol. 3, Atlantic City, NJ, Oct. 7-11, 2001, pp. 1256–1260.

[16] D. Kim, M. A. Ingram, and W. W. Smith, "Small-scale fading for an indoor wireless channel with modulated backscatter," in *Proc. 2001 IEEE 54th Veh. Technol. Conf.*, Atlantic City, NJ, Oct. 7-11, 2001, pp. 1616–1620.

[17] T. Helleseth and P. V. Kumar, "Pseudonoise sequences," in *The Mobile Communications Handbook*, J. D. Gibson, Ed. CRC Press, 1999, ch. 8.

[18] W. C. Jakes, *Microwave Mobile Communications*. IEEE Press, 1993.

[19] G. G. Raleigh and J. M. Cioffi, "Spatio-temporal coding for wireless communication," *IEEE Trans. Commun.*, vol. 46, pp. 357–366, Mar. 1998.

[20] M. Steinbauer, A. F. Molisch, and E. Bonek, "The double-directional radio channel," *IEEE Antennas Propag. Mag.*, vol. 43, pp. 51–63, Aug. 2001.

[21] L. M. Correia, *Wireless Flexible Personalised Communications*. John Wiley & Sons, 2001.

[22] Q. H. Spencer, B. D. Jeffs, M. A. Jensen, and A. L. Swindlehurst, "Modeling the statistical time and angle of arrival characteristics of an indoor multipath channel," *IEEE J. Sel. Areas Commun.*, vol. 18, pp. 347–360, Mar. 2000.

[23] B. D. Jeffs, E. Pyper, and B. Hunter, "A wireless MIMO channel probing approach for arbitrary antenna arrays," in *Proc. 2001 IEEE Intl. Conf. Acoust. Speech Signal Process.*, vol. 4, Salt Lake City, UT, May 7-11, 2001, pp. 2493–2496.

[24] R. Roy and T. Kailath, "ESPRIT – estimation of signal parameters via rotational invariance techniques," *IEEE Trans. Acoust. Speech Signal Process.*, vol. 37, pp. 984–995, Jul. 1989.

[25] J. Fuhl, J.-P. Rossi, and E. Bonek, "Highresolution 3-D direction-of-arrival determination for urban mobile radio," *IEEE Trans. Antennas Propag.*, vol. 45, pp. 672–682, Apr. 1997.

[26] H. Krim and M. Viberg, "Two decades of array signal processing research: The parametric approach," *IEEE Signal Process. Mag.*, vol. 13, pp. 67–94, Jul. 1996.

[27] M. Haardt and J. A. Nossek, "Simultaneous Schur decomposition of several nonsymmetric matrices to achieve automatic pairing in multidimensional harmonic retrieval problems," *IEEE Trans. Signal Process.*, vol. 46, pp. 161–169, Jan. 1998.

[28] A.-J. van der Veen and A. Paulraj, "An analytical constant modulus algorithm," *IEEE Trans. Signal Process.*, vol. 44, pp. 1136–1155, May 1996.

[29] I. De Coster, E. Van Lil, B. G. Loureiro, P. Delmotte, and A. Van de Capelle, "Validation measurements for the Fresnel approximation of the PO model," in *Proc. 28th. Eur. Microw. Conf.*, vol. 1, Amsterdam, The Netherlands, Oct. 5-9, 1998, pp. 463–468.

[30] R. B. Ertel, P. Cardieri, K. W. Sowerby, T. S. Rappaport, and J. H. Reed, "Overview of spatial channel models for antenna array communication systems," *IEEE Pers. Commun.*, vol. 5, pp. 10–22, Feb. 1998.

[31] K. I. Pedersen, J. B. Andersen, J. P. Kermoal, and P. Mogensen, "A stochastic multiple-input-multiple-output radio channel model for evaluation of space-time coding algorithms," in *Proc. 2000 IEEE 52nd Veh. Technol. Conf.*, vol. 2, Boston, MA, Sep. 24-28, 2000, pp. 893–897.

[32] A. M. Sayeed, "Modeling and capacity of realistic spatial MIMO channels," in *Proc. 2001 IEEE Intl. Conf. Acoust. Speech Signal Process.*, vol. 4, Salt Lake City, UT, May 7-11, 2001, pp. 2489–2492.

[33] D. Gesbert, H. Bölcskei, D. A. Gore, and A. J. Paulraj, "Outdoor MIMO wireless channels: Models and performance prediction," *IEEE Trans. Commun.*, vol. 50, pp. 1926–1934, Dec. 2002.

[34] D. J. Cichon and T. Kurner, "Propagation prediction models," in *COST 231 Final Rep.*, 1995, available online at http://www.lx.it.pt/cost231/.

[35] J. W. Wallace and M. A. Jensen, "Characteristics of measured 4x4 and 10x10 MIMO wireless channel data at 2.4-GHz," in *Proc. 2001 IEEE Antennas Propag. Soc. Intl. Symp.*, vol. 3, Boston, MA, Jul. 8-13, 2001, pp. 96–99.

[36] H. Özcelik, M. Herdin, W. Weichselberger, J. Wallace, and E. Bonek, "Deficiencies of 'Kronecker' MIMO radio channel model," *Electron. Lett.*, vol. 39, pp. 1209–1210, Aug. 7, 2003.

[37] T. Svantesson and J. W. Wallace, "Tests for assessing multivariate normality and the covariance structure of MIMO data," in *Proc. 2003 IEEE Intl. Conf. Acoust. Speech Signal Process.*, vol. 4, Hong Kong, Apr. 6-10, 2003, pp. 656–659.

[38] D. Zwillinger, Ed., *Standard Mathematical 's and Formulae*, 30th ed. CRC Press, 1996.

[39] J. Wallace, H. Özcelik, M. Herdin, E. Bonek, and M. Jensen, "Power and complex envelope correlation for modeling measured indoor MIMO channels: A beamforming evaluation," in *Proc. 2003 IEEE 58th Veh. Technol. Conf.*, vol. 1, Orlando, FL, Oct. 6-9, 2003, pp. 363–367.

[40] G. J. Foschini and M. J. Gans, "On limits of wireless communications in a fading environment when using multiple antennas," *Wireless Pers. Commun.*, vol. 6, pp. 311–335, Mar. 1998.

[41] S. Loyka and A. Kouki, "The impact of correlation on multi-antenna system performance: Correlation matrix approach," in *Proc. 2001 IEEE 54th Veh. Technol. Conf.*, vol. 2, Atlantic City, NJ, Oct. 7-11, 2001, pp. 533–537.

[42] K. Yu, M. Bengtsson, B. Ottersten, D. McNamara, P. Karlsson, and M. Beach, "A wideband statistical model for NLOS indoor MIMO channels," in *Proc. 2002 IEEE 55th Veh. Technol. Conf.*, vol. 1, Birmingham, AL, May 6-9, 2002, pp. 370–374.

[43] J. P. Kermoal, L. Schumacher, K. I. Pedersen, P. E. Mogensen, and F. Frederiksen, "A stochastic MIMO radio channel model with experimental validation," *IEEE J. Sel. Areas Commun.*, vol. 20, pp. 1211–1226, Aug. 2002.

[44] J. W. Wallace and M. A. Jensen, "Modeling the indoor MIMO wireless channel," *IEEE Trans. Antennas Propag.*, vol. 50, pp. 591–599, May 2002.

[45] J. Kermoal, L. Schumacher, F. Frederiksen, and P. Mogensen, "Polarization diversity in MIMO radio channels: Experimental validation of a stochastic model and performance assessment," in *Proc. 2001 IEEE 54th Veh. Technol. Conf.*, vol. 1, Atlantic City, NJ, Oct. 7-11, 2001, pp. 22–26.

[46] C. B. Peel and A. L. Swindlehurst, "Effective SNR for space-time modulation over a time-varying Rician channel," *IEEE Trans. Commun.*, vol. 52, pp. 17–23, Jan. 2004.

[47] D. Chizhik, G. J. Foschini, M. J. Gans, and R. A. Valenzuela, "Keyholes, correlations, and capacities of multielement transmit and receive antennas," *IEEE Trans. Wireless Commun.*, vol. 2, pp. 361–368, Apr. 2002.

[48] D. Gesbert, H. Bölcskei, D. A. Gore, and A. J. Paulraj, "Performance evaluation for scattering MIMO channel models," in *Conf. Rec. 34th Asilomar Conf. Signals Syst. Comput.*, vol. 1, Pacific Grove, CA, Oct. 29 - Nov. 1, 2000, pp. 738–742.

[49] D. W. Bliss, K. W. Forsythe, and A. F. Yegulalp, "MIMO communication capacity using infinite dimension random matrix eigenvalue distributions," in *Conf. Rec. 35th Asilomar Conf. Signals Syst. Comput.*, vol. 2, Pacific Grove, CA, Nov. 4-7, 2001, pp. 969–974.

[50] R. B. Ertel and J. H. Reed, "Angle and time of arrival statistics for circular and elliptical scattering models," *IEEE J. Sel. Areas Commun.*, vol. 17, pp. 1829–1840, Nov. 1999.

[51] A. Abdi and M. Kaveh, "A space-time correlation model for multielement antenna systems in mobile fading channels," *IEEE J. Sel. Areas Commun.*, vol. 20, pp. 550–560, Apr. 2002.

[52] O. Nørklit and J. B. Andersen, "Diffuse channel model and experimental results for array antennas in mobile environments," *IEEE Trans. Antennas Propag.*, vol. 46, pp. 834–840, Jun. 1998.

[53] G. L. Turin, F. D. Clapp, T. L. Johnston, B. F. Stephen, and D. Lavry, "A statistical model of urban multipath propagation," *IEEE Trans. Veh. Technol.*, vol. VT-21, pp. 1–9, Feb. 1972.

[54] A. A. M. Saleh and R. A. Valenzuela, "A statistical model for indoor multipath propagation," *IEEE J. Sel. Areas Commun.*, vol. SAC-5, pp. 128–137, Feb. 1987.

[55] A. F. Molisch, "A generic model for MIMO wireless propagation channels," in *Proc. 2002 IEEE Intl. Conf. Commun.*, vol. 1, New York, Apr. 28 - May 2, 2002, pp. 277–282.

[56] C.-C. Chong, C.-M. Tan, D. I. Laurenson, S. McLaughlin, M. A. Beach, and A. R. Nix, "A new statistical wideband spatio-temporal channel model for 5-GHz band WLAN systems," *IEEE J. Sel. Areas Commun.*, vol. 21, pp. 139–150, Feb. 2003.

[57] T. Zwick, C. Fischer, D. Didascalou, and W. Wiesbeck, "A stochastic spatial channel model based on wave-propagation modeling," *IEEE J. Sel. Areas Commun.*, vol. 18, pp. 6–15, Jan. 2000.

[58] J. Fuhl, A. F. Molisch, and E. Bonek, "Unified channel model for mobile radio systems with smart antennas," *IEE Proc. Radar Sonar Navigation*, vol. 145, pp. 32–41, Feb. 1998.

[59] M. Stege, J. Jelitto, M. Bronzel, and G. Fettweis, "A multiple input-multiple output channel model for simulation of Tx- and Rx-diversity wireless systems," in *Proc. 2000 IEEE 52nd Veh. Technol. Conf.*, vol. 2, Boston, MA, Sep. 24-28, 2000, pp. 833–839.

[60] T. Kurner, D. J. Cichon, and W. Wiesbeck, "Concepts and results for 3D digital terrain-based wave propagation models: An overview," *IEEE J. Sel. Areas Commun.*, vol. 11, pp. 1002–1012, Sep. 1993.

[61] H. L. Bertoni, W. Honcharenko, L. R. Macel, and H. H. Xia, "UHF propagation prediction for wireless personal communications," *Proc. IEEE*, vol. 82, pp. 1333–1359, Sep. 1994.

[62] S. Y. Seidel and T. S. Rappaport, "Site-specific propagation prediction for wireless in-building personal communication system design," *IEEE Trans. Veh. Technol.*, vol. 43, pp. 879–891, Nov. 1994.

[63] G. E. Athanasiadou, A. R. Nix, and J. P. McGeehan, "A microcellular ray-tracing propagation model and evaluation of its narrow-band and wide-band predictions," *IEEE J. Sel. Areas Commun.*, vol. 18, pp. 322–335, Mar. 2000.

[64] M. F. Iskander and Z. Yun, "Propagation prediction models for wireless communication systems," *IEEE Trans. Microw. Theory Tech.*, vol. 50, pp. 662–673, Mar 2002.

[65] Y. Wang, S. Safavi-Naeini, and S. K. Chaudhuri, "A hybrid technique based on combining ray tracing and FDTD methods for site-specific modeling of indoor radio wave propagation," *IEEE Trans. Antennas Propag.*, vol. 48, pp. 743–754, May 2000.

[66] Z. Zhang, R. Sorensen, Z. Yun, M. F. Iskander, and J. F. Harvey, "A ray-tracing approach for indoor/outdoor propagation through window structures," *IEEE Trans. Antennas Propag.*, vol. 50, pp. 742–748, May 2002.

[67] A. L. Swindlehurst, G. German, J. Wallace, and M. Jensen, "Experimental measurements of capacity for MIMO indoor wireless channels," in *IEEE Third Workshop Signal Process. Adv. Wireless Commun. 2001. (SPAWC '01)*, Taoyuan, Taiwan, R.O.C. Mar. 2001, pp. 30–33.

[68] H. Zhu, J. Takada, and T. Kobayashi, "The verification of a deterministic spatio-temporal channel modeling approach by applying a deconvolution technique in the measurement," in *Proc. 2001 IEEE 53rd Veh. Technol. Conf.*, vol. 1, Rhodes, Greece, May 6-9, 2001, pp. 362–366.

[69] A. Muller, "Monte-carlo multipath simulation of ray tracing channel models," in *Proc. 1994 IEEE Global Telecomm. Conf.*, vol. 3, San Francisco, CA, Nov. 11 - Dec. 2, 1994, pp. 1446–1450.

[70] R. A. Valenzuela, "Ray tracing prediction of indoor radio propagation," in *Proc. 1994 IEEE 5th Intl. Symp. Pers. Indoor Mobile Radio Commun.*, vol. 1, The Hague, The Netherlands, Sep. 18-23, 1994, pp. 140–144.

[71] P. Marques, J. Fernandes, and J. Neves, "Complex impulse response modeling for wideband channels," in *Proc. 1998 IEEE Spring Veh. Technol. Conf.*, vol. 2, Ottawa, Ontario, Canada, May 18-21, 1998, pp. 702–706.

[72] K. R. Dandekar, A. Arredondo, G. Xu, and H. Ling, "Using ray tracing to study urban vector channel propagation characteristics," in *Proc. 1999 IEEE Spring Veh. Technol. Conf.*, vol. 1, Houston, TX, May 16-20, 1999, pp. 381–385.

[73] C.-N. Chuah, D. N. C. Tse, J. M. Kahn, and R. A. Valenzuela, "Capacity scaling in MIMO wireless systems under correlated fading," *IEEE Trans. Inf. Theory*, vol. 48, pp. 637–650, Mar. 2002.

[74] F. Tila, P. R. Shepherd, and S. R. Pennock, "Theoretical capacity evaluation of indoor micro- and macro-MIMO systems at 5 GHz using site specific ray tracing," *Electron. Lett.*, vol. 39, pp. 471–472, Mar. 6 2003.

[75] J.-H. Jo, M. A. Ingram, and N. Jayant, "Angle clustering in indoor space-time channels based on ray tracing," in *Proc. 2001 IEEE 54th Veh. Technol. Conf.*, vol. 4, Atlantic City, NJ, Oct. 7-11, 2001, pp. 2067–2071.

[76] C. Martin, J. Winters, and N. Sollenberger, "MIMO radio channel measurements: Performance comparison of antenna configurations," in *Proc. 2001 IEEE 54th Veh. Technol. Conf.*, vol. 2, Atlantic City, NJ, Oct. 7-11, 2001, pp. 1225–1229.

[77] R. G. Vaughan and J. B. Andersen, "Antenna diversity in mobile communications," *IEEE Trans. Veh. Technol.*, vol. VT-36, pp. 147–172, Nov. 1987.

[78] T. Svantesson, "Correlation and channel capacity of MIMO systems employing multimode antennas," *IEEE Trans. Veh. Technol.*, vol. 51, pp. 1304–1312, Nov. 2002.

[79] C. Waldschmidt, T. Fugen, and W. Wiesbeck, "Spiral and dipole antennas for indoor MIMO-systems," *IEEE Antennas Wireless Propag. Lett.*, vol. 1, no. 1, pp. 176–178, 2002.

[80] T. Svantesson, M. A. Jensen, and J. W. Wallace, "Analysis of electromagnetic field polarizations in multi-antenna systems," *IEEE Trans. Wireless Commun.*, vol. 3, pp. 641–646, Mar. 2004.

[81] R. A. Andrews, P. P. Mitra, and R. deCarvalho, "Tripling the capacity of wireless communications using electromagnetic polarization," *Nature*, vol. 409, pp. 316–318, Jan. 2001.

[82] J. B. Andersen and B. N. Getu, "The MIMO cube - a compact MIMO antenna," in *Proc. 5th Intl. Symp. Wireless Pers. Multimedia Commun.*, vol. 1, Honolulu, HI, Oct. 27-30, 2002, pp. 112–114.

[83] T. Svantesson and A. Ranheim, "Mutual coupling effects on the capacity of multielement antenna systems," in *Proc. 2001 IEEE Intl. Conf. Acoust. Speech Signal Process.*, vol. 4, Salt Lake City, UT, May 7-11, 2001, pp. 2485–2488.

[84] C. Waldschmidt, J. v. Hagen, and W. Wiesbeck, "Influence and modeling of mutual coupling in MIMO and diversity systems," in *Proc. 2002 IEEE Antennas Propag. Soc. Intl. Symp.*, vol. 3, San Antonio, TX, Jun. 16-21, 2002, pp. 190–193.

[85] B. Clerckx, D. Vanhoenacker-Janvier, C. Oestges, and L. Vandendorpe, "Mutual coupling effects on the channel capacity and the space-time processing of MIMO communication systems," in *Proc. 2003 IEEE Intl. Conf. Commun.*, vol. 4, Anchorage, AK, May 11-15, 2003, pp. 2638–2642.

[86] D. M. Pozar, *Microwave Engineering*. John Wiley & Sons, 1998.

[87] J. Engberg and T. Larsen, *Noise Theory of Linear and Nonlinear Circuits*. John Wiley & Sons, 1995.

[88] G. Gonzalez, *Microwave Transistor Amplifiers*. Prentice-Hall, 1997.

[89] J. W. Wallace and M. A. Jensen, "Mutual coupling in MIMO wireless systems: A rigorous network theory analysis," *IEEE Trans. Wireless Commun.*, vol. 3, pp. 1317–1325, Jul. 2004.

[90] J. W. Wallace and M. A. Jensen, "The capacity of MIMO wireless systems with mutual coupling," in *Proc. 2002 IEEE 56th Veh. Technol. Conf.*, vol. 2, Vancouver, British Columbia, Canada, Sep. 24-28, 2002, pp. 696–700.

[91] A. Taflove and S. C. Hagness, *Computational Electrodynamics: The Finite-Difference Time-Domain Method*, 2nd ed. Artech House, Boston, 2000.